BANDING IN NICKEL-BASE SUPERALLOYS AND STEELS

by

Ting Li

B. Eng., University of Science and Technology, Beijing, 2004

A THESIS SUBMITTED IN PARTIAL FULFILLMENT OF
THE REQUIREMENTS FOR THE DEGREE OF

MASTER OF APPLIED SCIENCE

in

The Faculty of Graduate Studies

(Materials Engineering)

THE UNIVERSITY OF BRITISH COLUMBIA

December 2007

Abstract

Process irregularities in remelting furnace operation have an impact on the ingot solidification structure which depends on the local thermal conditions and the alloy concerned. In this work, a laboratory investigation into the structures resulting from interruptions in solid growth is presented in order to understand the cause and effect relationship between the solidification interruption and banding. The results demonstrate the range of structure, segregation and precipitation changes which are experienced by a range of alloys including Inconel 718, Nimonic 80A, Waspaloy and M50. In the case of alloys which form primary precipitates, the interruption period is shown to give rise to structure changes. Segregations are found due to the interruption. We also comment on the differences observed between industrial examples of banding and the laboratory samples which may be due to the absence of liquid movement in the latter technique. It is concluded that the interruption in solidification condition during a directionally solidification itself can produce banding through its effects on the morphology of precipitates.

Table of Contents

List of Tables

List of Figures

Acknowledgements

The author would like to thank particularly her supervisor, Dr. A. Mitchell, for his guidance through this M.A.Sc.

A special thank should go to the author's co-supervisor Dr. S. L. Cockcroft for his innumerable helpful advice during this work.

The author is very thankful to Dr. A. Akhtar for his assistance and invaluable support throughout the duration of this work.

All the support staff in the department of Metals & Materials Engineering at UBC was also most helpful.

1. Introduction

Banding, also called tree rings, is a defect or anomaly observed in steel and other alloy products in which alternating bands of different structures develop. These differences can be attributed to alternating structures on a micro or macro scale, differing elemental compositions, and in some cases, distinct grain types [1]. This phenomenon has been studied extensively because it can result in a deterioration of the mechanical properties, poor machineability, uneven response to surface hardening, heat treatment distortion, poor corrosion resistance, cold cracking and poor impact resistance [2]. In addition, tree-ring structures are of interest because they have been associated with the occurrence of other ingot defects [3, 4]. The banding structures observed frequently in VAR and ESR ingots have been simulated and examined in the present work.

Efforts to eliminate the banding defect in the ingots by homogenizing at a high temperature proved to be impractical industrially [5]. The temperature, 1300 ℃ for instance, which is needed to remove the associated segregation through diffusion in a reasonable time period is high. This high temperature can result in structural damage through "overheating" i.e. grain boundary liquidation. A lower temperature homogenization would require holding ingots for extremely long times, for example, two weeks, which would not be cost effective in practice. Therefore, once banding

appears in the ingot product, it is common industrial practice to crop the portion of the ingot containing the bands rather than process the entire ingot further.

Solidification instability can form alternating structures or phases which develop mostly parallel to the S/L front [6, 7]. Those structures are called internal banding. Such banded structures are observed in several peritectic systems. Kurz *et al* [6] have stated that internally driven bands form due to reactions at the solid-liquid interface. They investigated the origin of inherent banded patterns of low velocity peritectic solidification as well as high velocity non-equilibrium solidification, and concluded that banding is produced at a low interface velocity due to the nucleation of another phase at the growing interface during the establishment of a steady state growth condition. The unique solidification process of the peritectic system plays a role in the process. The solid solution phase γ is precipitated through a reaction between the liquid phase(L) and the higher temperature phase δ. Oscillatory transformation alternating between δ and γ can give rise to a banded structure parallel to the S/L interface.

Non-equilibrium banded structures have also been observed at high growth rates. At those high rates of growth, the solute can not diffuse efficiently. This type of banded structure forms due to the loss of local equilibrium at the interface and is not restricted to any specific type of phase diagram. The banded microstructure is thought to be formed by an oscillatory exchange of two different solidification growth

morphologies, i.e. dendrites and plane front. Kurz *et al* [6] observed a transition at a critical growth rate, above which the steady-state growth of the columnar dendrites gave rise to an oscillatory instability of the solid/liquid interface. These oscillations created the light and dark bands which are approximately parallel to the S/L interface.

Although banding may be caused by the internal instability which happens during solidification as illustrated above, external irregularities happening during production process can also produce tree-ring structures. During an industrial remelting process, such as VAR or ESR, it is difficult to maintain a stable melting/freezing status throughout the entire production, which would amongst other things require the provision of a perfect electrode (as opposed to one containing the normal structural defects such as inclusion and porosity). The maintenance of a constant heat balance is a delicate operation requiring critical decisions on the part of the operator regarding control response and choice of operating parameters. Therefore process instabilities can easily occur and cause the formation of tree rings in ingots[8]. In both ESR and VAR processes, banding in the ingot results from instabilities either inherent in the solidification process or caused by a disruption in the processing parameters. Therefore this type of defect can be eliminated in principle by correct conduct of the process, nonetheless it is important to understand both the mechanisms and the structural consequences of the effect. With that knowledge, it may also be possible to alter the process parameters so as to move the solidification conditions

toward conditions that are conducive to greater stability at the solid/liquid (S/L) interface.

Clearly, there exists a need for a better understanding of the mechanism or mechanisms responsible for the formation of tree rings. The focus of the present work is to examine in detail features present in industrial ingots containing bands, and, to shed light on the mechanisms responsible for their formation through conducting laboratory experiments under controlled conditions of solidification.

2. Literature Review

2.1 Theories on Banding Formation

There is no universally accepted definition of banding because various micro/macro structures and features can give rise to this type of structure. Moreover, there are clearly a variety of mechanisms by which they can form. However, there have been several attempts to better define this phenomenon. Banding is considered by Krauss [1] to be a microstructural condition in which alternating bands of different microstructures develop in alloy products. It is usually a region consisted of columnar dendrites, in which the content of solute elements is different from the normal bulk. It may also contain equiaxed grains. Sawa *et al* [8] observed tree-ring patterns consisting of "white stripes" on a macro-etched surface of a section taken from a VAR ingot. They also indicated that bands are composed of fine equiaxed crystals, in which the contents of the solute elements are lower than in the adjacent "normal" material.

Theories have also been forwarded since early in the twentieth century to explain the mechanism responsible for the formation of the banded structures. The early theories invoked the concept of a reaction taking place in the "Inclusion" and "phosphorous" [9-11]. Banding was thought to be caused by the uneven distribution of inclusion or phosphorous in the alloy. However, progress in metallurgical processes has rendered these descriptions of historical interest only. They have essentially no relevance to the present work except to emphasize the fact that banding has been an

industrial problem for a long time. More recent studies have provided better insight. Jatczak *et al* [12] studied the banding phenomenon in AISI steels of the type1340, 2340, 4140, 4340 and 5140 and indicated that chemical heterogeneity produces visible banding through its effect on nucleation and growth of ferrite and pearlite from austenite. In other words, the primary cause of banding in steels is the effect of alloy segregation on carbon-rich location. In their analysis, carbide forming type elements, for example, Cr tended to increase the carbon concentration in their vicinity whereas, elements like nickel which have a large carbon solubility, tended to decrease carbon concentration in their vicinity. Therefore, the degree of carbon segregation and the location of high and low carbon areas depend only on the amount and distribution of the alloying elements. In multi-alloyed steels, these visual banded conditions depend upon the influence of the various types of alloying elements, their amounts and distribution. Bastien [13] concluded that in steels each element which remains in solid solution and produces a displacement of the Ar_3 temperature (i.e. Austenite decomposition temperature) can give rise to a banded structure. For example, if this temperature is lowered by the solute, then proeutectoid ferrite nucleates first in the solute lean region. Otherwise, if this temperature is raised, the preeutectoid ferrite nucleates in the solute rich region. In either case, carbon atoms are rejected from the proeutectoid ferrite, thus producing carbon rich regions of austenite, which eventually transform to pearlite. In addition, he investigated the effect of cooling rate on the appearance of banded structure, and it was found that increasing the cooling rate in carbon and low-alloy steels of the hypoeutectic type resulted in the banded region

disappearing. Kirkaldy *et al* [14] designed a series of experiments for the purpose of finding out which theory, Jatczak's [12] or Bastien's [13], is correct. The results showed that the dominant effect in producing microstructural banding is the constitutional effects of alloying elements in shifting Ar_3 lines as proposed by Bastien. Thompson and Howell [15] investigated the effect of austenite grain size as well as the cooling rate on the propensity for microstructure banding in a low-alloy steel, and found that the banding disappeared when the austenite grain size was 2-3 times larger than the banding wavelength. In addition, the microstructural banding areas were still present when the austenite grain size was considerably less than the banding wavelength. As for cooling rate, it was proposed that the intensity or degree of microstructural banding increases as cooling rate decreases. Lavender and Jones [5] investigated the photomicrographs and microradiographs of banding in ASTM type G 122, G 136, G 663 and G 684 steels and calculated the temperature required to remove banding. They concluded that a high temperature treatment in the range of 1200-1350 ℃ could remove banding. In all the cases they investigated, the high temperatures would also result in overheating of the steel. As noted earlier, heat treatment as a method of removing banding cannot be considered of practical interest. Based on a sinusoidal variation of composition, they also claimed that several hundred years would be required to remove the segregates at a relatively lower temperature, such as 625 ℃. Krauss [1] concluded from his work that the root cause of banding is residual interdendritic microsegregation. Although segregation was found to be almost always present irrespective of the formation of bands, the microstructural manifestations of

banding depended on austenite grain size and cooling conditions that control austenite decomposition to other phases.

The following theories have been proposed to explain macroscopic banding in casting and remelting processes. Sawa *et al* [8] considered that the origin of tree-ring structure is the alteration of solidification condition caused by the change of magnetic stirring intensity. They observed a fine equiaxial structure within the tree-rings in which the presence of eutectic carbides could not be detected. It was proposed that this segregation is formed by solidification taking place earlier than in the vicinity possibly due to either the nucleation of equiaxial crystals or deposition of fragments of dendrites in a thin layer near the solidification front under the change of the stirring intensity. Jackson [16] proposed a model for the formation of the carbon concentration bands during the "power-on-off" sequence of a remelting process. Two process transients were examined; turning the power off, and turning the power on. In the first transient, the solidification rate would gradually increase as the liquid pool shrinks from the steady state profile. When power supply is turned back on, the melt rate of the electrode would be higher than its equilibrium value, resulting in a deeper liquid metal pool profile. Finally, the system would try to return to its equilibrium, which requires the increase of the solidification rate in the center region of the ingot. Increased solidification rate would force the effective distribution coefficient (Ke) for carbon in the system to approach unity. As the value of Ke increases, the concentration of carbon in the solid metal would be increased. Lee *et al* [4] investigated

the banded structure on nickel-based superalloy Inconel 718. In their description, banding is observed as strings of equiaxed grains interrupting a predominately columnar-dendritic structure. They stated that this structure forms due to a transient caused by process perturbation at the solidification front. Furthermore, they concluded that grains inside the tree-ring must have formed by a nucleation mechanism which occurs due to the perturbation in the thermal and solutal field ahead of the mushy zone. It was suggested that this perturbation could be caused by either a reduction in the convective flow so that less heat could be supplied by the liquid above or through a reversal of the flow carrying cooler liquid from the central zone of the ingot along the front of the columnar mushy zone. A third mechanism considered plausible was a change in the flow direction, such that the solute-rich liquid is replaced by the bulk liquid from the pool.

Electromagnetic stirring on the formation of band in continuous casting has been investigated extensively [17-24]. For instance, Shah and Moore [19] studied in detail the solidification morphology and "white band" formation in continuously cast steels. They attributed the columnar-equiaxed transition to the convective fluid flow. Strong convective fluid can detach parts of the mushy zone due to diffusion of dendrite heads or simply break off dendrite tips. The detached dendrite particles may then act as nuclei for the formation of equiaxed crystallization. Stirring can arrest the columnar crystallization and promote the formation of a fine and columnar equiaxed zone. Also, when the stirring power is too high, a band of negative segregation will appear at the

limit of the columnar crystals. It was suggested that the bands of negative segregation are produced by the solute-enriched liquid being swept away from the solidification front by the effect of the stirring motion and the arresting of the columnar solidification front. Another study on the formation of the band segregation during the electromagnetic stirring of a strand-cast steel has been done by Bridge and Rogers[22]. They described banding as a white band with negative segregation corresponding to the position of the solidification front during stirring. Following hot working of the material containing the white bands can act as an obstacle to the customer acceptance of the product. Calculations have demonstrated that the observed segregation could arise as a result of changes in the velocity of the liquidus front at the start and end of stirring. These velocity changes are caused primarily by a change in thermal conditions at the liquidus resulting in a slowing down and subsequent speeding up of the isotherm. Some solute depleted bands were observed when aluminum –gold alloys were partially remelted and then held under a constant temperature gradient. Beech [23] studied this phenomenon and the conclusions made were summarized as shown in Figure 2.1. During the casting, the cells may be represented as in (a). On rapid remelting, the liquidus isotherm will retreat faster than the solidus in the steeper temperature gradient (line A in (c)). As remelting ceases and the furnace stabilizes, the temperature gradient decreases (line B in (c)). This causes the cells to grow into the liquid and remelting occurs further into the cell roots leading to an increase in the apparent liquid plus solid zone. In addition, solute will diffuse towards the bulk liquid creating a concentration distribution within the interdendritic liquid, as shown in (b).

Stabilization and solute diffusion from between the cells would cause the initial band to widen and become solute depleted. Zanner *et al*[24] analyzed the origin of tree-ring formation in VAR ingots. According to their observation, it is very likely that either the sudden stirring of the melt or the electromagnetic fluctuations is the cause of VAR banding. In the former case, the high liquid velocity created by the stirring coil swept away the Nb rich liquid leaving a depleted region. In the latter case, if the pathway for current undergoes periodic fluctuations, then the fluctuations in the spatial distributions of Lorenz force could lead to fluctuations in the local intensity or direction of flow in the pool. Given that the liquidus isotherm velocity is influenced by the temperature and composition of the liquid flowing past the dendrite tips, changes in the fluid velocity profile within the pool could easily lead to composition banding.

2.2 The Influence of Banding on Mechanical Properties

Mechanical properties are influenced by the heterogeneity caused by banding. The impact of banding varies among different types of alloys. Schwartzbart [25] investigated the mechanical properties of a 0.21 wt% carbon, 1.47 wt% manganese steel which exhibited severe manganese banding. The transverse mechanical properties of the bulk material improved through manganese homogenization which removed this variation. Working on a heavily banded 0.3 % carbon steel, Jatczak *et al* [12], however, concluded that homogenization causes little alteration in longitudinal mechanical properties, and only slight, commercially insignificant, improvements in

the transverse ductility and impact strength. Owen *et al*[26] compared the behavior of low-carbon steel with banded and homogenized microstructures and found no difference in impact properties below the ductile to brittle transition temperature. However, in the testing temperature range for ductile fracture, both longitudinal and transverse energy absorptions were higher in homogenized specimens. Grange [27] concluded that both microstructural banding and elongated inclusions cause anisotropy in mechanical properties in wrought (0.25 wt%C and 1.5 wt%Mn) steel. Elimination of banding was effective in reducing anisotropy but resulted in only slight improvement of anisotropy in the steel containing many elongated inclusions. Heiser and Hertzberg [28] found that the ductility and impact-resistance anisotropy in banded steel was controlled by the delaminations which occurred by inclusion/matrix interface separation in the mechanically fibred material. When delamination occurs normal to the growth direction, they are beneficial, by increasing the fracture energy and ductility, but when they occur in the growth direction and on the fracture plane, they are detrimental. Rao [29] studied the influence of banding on the impact and fatigue properties of a high strength SAE steel and concluded that the elimination of banding brought about an increase in impact strength and fatigue properties, and this was more pronounced at lower temperatures than at higher temperatures. The endurance limit was also raised by 8 % by the removal of banding. Jackson [16] found that in AISI 630 grade stainless steel banding consists of ferrite rich bands with the ferrite particles having higher concentration of chromium and lower concentration of nickel and copper. The bands contained 19 percent ferrite, which is higher than the specified

range of 5 to 7 percent. Cracks originated along the ferrite rich banded structure during rolling. Stauffer *et al* [30] examined low alloy steels. The presence of significant amounts of manganese, chromium, and molybdenum were found in the interdendritic region thus causing the segregated bands. Tensile testing of specimen oriented in the short transverse direction of the plate showed low ductility and a large variation in failure strains, depending on the continuity of the bands as well as the presence of large precipitate particles within the bands. Crack initiation in line pipe service failures has been traced to martensitic or hard segregation bands outcropping on the pipe surface [21] . It is known that hydrogen diffuses to the site of inclusions which exist in the macro-segregated regions causing catastrophic in-service failures.

2.3 ESR and VAR Industrial Processes

Since banding in ESR and VAR ingots is the focus of the present work, an overview of these two remelting processes is presented below.

2.3.1 ESR

Electroslag Remelting (ESR) is regarded as a method of refining metals using a molten slag that is electrically heated by its resistance [31] .This process has the advantage of being able to control both the composition and the microstructure of the ingot.

In an ESR process, the metal to be refined is usually in the form of an electrode, which is the product of a more conventional process. The lower end of an electrode is submerged in a bath of molten slag contained in a water-cooled mould. A schematic diagram of the process is shown in Figure 2.2. The required heat is generated by the electric current flowing between the electrode and the conducting baseplate on which the mould stands. As the slag temperature rises above the melting temperature of the metal, the tip of the electrode melts and thus collecting into droplets, being refined by reacting with the slag before falling through it and being collected in a pool in the mould. By matching of the melt rate to the cooling rate, conditions can be established to produce the desired microstructure.

The overall heat balance in ESR process has been illustrated by numerous workers. Figure 2.3 illustrates the nature of heat transfer[32]. Clearly, the heat flow is quite complicated. About one third of the energy input to the system is used in melting the metal[31]. The superheated droplets supply the major part of the heat at the ingot top. Heat removal from the ingot is mainly via the mould walls, and the heat transfer coefficient at this site is greatly dependent on the extent to which a contraction gap has appeared between the ingot and the mould.

Instability occurs during production. There are two main root causes of the instability, inconsistency in the movement of the slag and inability to control the position of the electrode. The interaction of two forces i.e. Lorenz force and buoyancy

force, changes strongly as the electrode/slag contact varies. Any changes in the process operation will immediately influence solidification and result in quality problems in the ingot [33] . The second cause of the instability, namely the control of electrode position, may be considered next. The magnitude of the interfacial resistance due to the contact of the electrode on the slag is dependent on current density and so it changes as the contact area varies with time. It is reasonable to anticipate that in a practical system used to control the electrode such an ill-defined control parameter can be incorrectly used, causing the electrode position to vary over an unacceptable range. If this change is sufficiently severe, the ingot thermal profile will vary and thus leading to segregation defects. Instability problem may also occur due to a change in the ambient atmosphere. Some industrial ESR melting processes are carried out under argon instead of air in order to minimize oxidation. The presence of argon stabilizes arc formation in the non-contact area between the electrode tip and the slag surface, leading to wrong response of the electrode movement, hence to a sharp change in the ingot thermal regime.

2.3.2 VAR

Vacuum arc remelting (VAR) is the principal, secondary melting process used to produce ingots of nickel-based alloys and of high quality steels [4] . The aim of VAR is to produce an ingot that is free of macrosegregation, porosity, shrinkage cavities, or any other defects resulted from solidification during conventional casting. In the VAR process, a cylinder-shaped, alloy electrode (usually prepared by conventional casting)

is loaded into the water-cooled, copper crucible of a VAR furnace, the furnace is evacuated, and a direct current arc is struck between the electrode (cathode) and some starting material and the electrode tip, eventually melting both. As the electrode tip is melted away, molten metal drips off forming a melt pool. The solidification profile is shown schematically in Figure 2.4 [4].

The general principle of the process is similar to that in ESR, but with many differences in detail. VAR can be operated to give higher cooling rates in the ingot and hence to provide less segregation than does ESR [34]. The general heat transfer is shown schematically in Figure 2.5. During this process, 50 % of the heat input is removed by the mould cooling water [35]. Without the insulating effect of the slag skin against the mold wall, the VAR ingot has a higher cooling rate than ESR, leading to generally shallower pools at the same melting rates and hence to products which contains less segregation [34]. An additional feature of VAR is that He (g) may be injected into the gap which develops between the mold wall and the contacting, solidifying ingot. The additional conduction effect of He increases ingot heat loss and further increases the ingot temperature gradients thus enhancing the tendency to reduced segregation.

The VAR process is inherently unstable [33]. Any change to the current, for example the momentary interruption of primary power input by an electrical event such as lightning storms, will abruptly change the two dominant forces (i.e. buoyancy

force and electromagnetic force) which control the flow pattern, thus giving rise to a change in pool profile. In general the operating system remains successful in preventing any significant excursions from the intended pool profile. However, if the parameters are incorrectly chosen instability can occur. Instability results from the electrode containing cracks, cavities or slag which abruptly change the arc behavior. The system may not be able to respond sufficiently quickly so as to prevent an abrupt change in the ingot heat balance. Also, the change of arc behavior can influence the voltage and current, thus changing the electromagnetic force on the ingot pool, resulting in a change of the heat balance at the liquidus. In addition, the electrode movement may not match the melting rate and so permit the arc length to extend. The heat balance is then changed to reflect an energy concentration at a single point, which distorts the normal parabolic shape which contains a depression on the "hot" side and a shallow region on the "cold" side. This effect has been modeled by Zanner *et al*[24] . Figure 2.6 shows the melt rate and the current across the radius of the ingot. Parts of the ingot will have undergone a freeze/remelt sequence, which may lead to segregation defects. The constricted arc condition is also frequently associated with the presence of electrode cavities, and hence with the formation of the white spot defect in the ingot. There are also other features during VAR process which can give rise to instability. Failing of the ingot to maintain contact with baseplate due to the cooling and contracting of the ingot's lower section. The use of helium which is injected into the mold/ingot gap as a coolant is another factor.

2.3.3 Solidification Conditions

The modeling of the remelting process is of great interest due to the important role of these processes played in steel and alloy-making industry. Based on the knowledge of the heat transfer and fluid flow mentioned earlier, a number of computing models [36-41] have been formulated by applying different numerical and analytical methods.

Ballantyne [39] applied an implicit finite difference technique. Problems involve the solution of two-dimensional partial differential equations subject to specified initial and boundary conditions. A more comprehensive computational model for the prediction of the performance of the ESR process was presented by Kelkar *et al* [40, 41] for axisymmetric, steady state conditions, using a Computational Fluid Dynamics (CFD) approach and modeling the slag simultaneously with the ingot. There are several differences between the two models mentioned above. One difference lies in their solution to the liquid pool conductivity. In the finite difference model, deducted by Ballantyne, in order to account for the liquid movement, an elevated liquid pool conductivity has to be assumed which is not true in reality. On the other hand, Kelkar's model computes the effective conductivity using a turbulence model, which is more accurate. Another difference between these two models is the consideration of the heat flow in the slag. Ballantyne's assumption on temperature distribution across the top of the ingot does not have anything to do with the temperature and heat flow within the slag. Kelkar's model is more accurate because it calculates the thermal

profile of the slag instead of making an assumption about it. In spite of the advantages of Kelkar's model over Ballantyne's, the results of the model are not very different. Figure 2.7 [41] and Figure 2.8 [40] show the temperature distribution acquired in the ESR (Inconel 718) and VAR (Ti-64) ingots respectively. Kelkar's model had been used in the computations of the two profiles mentioned above. Models and experiments have also been developed to predict the primary dendrite arm spacing as well as the transition from one morphology to another for different solidification rates and temperature gradients. The results reported in the literature are show in Figure 2.9 [42] and Figure 2.10 [43].

During the remelting process, the sudden power interruption can cause the change of solidification condition. Jackson [16] investigated the heat transfer and thermal behavior of VAR and ESR ingots during power-off mode. His conclusion is summarized below: There are four main areas affected by the loss of heat input caused by the power interruption. They are: liquid metal/slag skin interface, liquid slag/slag skin interface, liquid slag/atmosphere interface and liquid metal/liquid slag interface. For the first three, the results show that the rate of heat loss from these interfaces drops off very rapidly and that they respond instantaneously to the "power-off" condition. The heat transfer across the slag/metal interface is dependent on the value of the heat transfer coefficient due to the small temperature gradient across the interface. This heat supply would reduce the extent of the solidification in

the metal pool. The process finally resulted in a tree-ring structure as mentioned earlier.

3. Objectives and Scope

The objective of this work is to enhance the understanding of the cause and effect relationship between the solidification interruption and banding. In order to achieve this objective, two industrial samples as well as seven laboratory-produced samples were investigated. Industrial samples include an as-cast Inconel 718 sample and a forged Waspaloy sample. Both these samples contain banding in their structures. The laboratory-produced samples were made as a part of this investigation. Castings using four materials, including three nickel-base superalloys (Inconel 718, Nimonic 80A and Waspaloy) and one tool steel (M50) were produced under a variety of solidification conditions. The scope of the present work includes is microstructure investigations and compositional analyses. Investigations were performed using optical microscopy and scanning electron microscopy.

4. Materials and Experimental Procedure

4.1 Materials

Samples of the industrial ingots received as well as the specimens prepared in the laboratory were made of three nickel based superalloys (Inconel 718, Nimonic 80A and Waspaloy) and a steel (M50). Their nominal compositions are shown in Table 4-1. The industrial specimens were made of Inconel 718 and Waspaloy. The choice of those four compositions was made based on their solidification characteristics. Inconel 718 has a segregated interdendritic liquid which is heavier than the bulk liquid. For Waspaloy and Nimonic 80A, however, the segregating liquid would be lighter than the bulk liquid. If there is significant flow of the interdendritic liquid during an interruption in solidification, the alloys should show corresponding observable differences in the bulk composition. The choice of M50 was made on the basis that it shows a wider gap between dendrites than do superalloys. In addition, M50 precipitates various carbides under different cooling conditions, which makes it possible to understand the solidification mechanism through observations made on the type of carbide formed. An overview of each of the four alloys with emphasis on its solidification characteristics follows.

4.1.1 Inconel 718

Superalloys have been developed in order to meet the demand of increasing high temperature application. The required properties of this special species are the strength and corrosion resistance at high temperature. Inconel 718 (Inconel is a registered trademark of Special Metals Group of Companies, designated as UNS N07718) represents the most widely used alloy for turbine vanes and discs in aero-engine applications with working temperatures up to 700 ℃ [44].

Inconel 718 is a precipitation-strengthened nickel-iron-base superalloy. The reactions occurring upon cooling and the phases generated as a result are summarized in Table 4-2 [45, 46] . The process of strengthening is primarily achieved through the precipitation of γ'' with a secondary hardening taking place through the precipitation of γ' [47] . Another strengthening phase, the δ phase, prevents grain growth through being precipitated on the grain boundaries [48]. The obvious advantages of this alloy lie in that it has good strength, corrosion resistance and ductility, good weldability, along with long time stability within the working temperature range and has only a few critical alloying elements. With the improvement of casting technique, large components of Inconel 718 have been made cost effectively which has further promoted its usage [44] .

The melting range of Inconel 718 is 1336 ℃ to 1260 ℃. The solidification of Inconel 718 starts with the proeutectic γ reaction at about 1336 ℃, followed by the

precipitation of (Ti,Nb)C inside the dendrites at 1290 ℃. The (γ + Laves phase) eutectic reaction occurs at about 1175 ℃, and the δ phase precipitation happens at about 1145 ℃. The final γ' and γ'' precipitation occurs at 1000 ℃ [46].

The solidification structure and the associated precipitates encountered in the final microstructure of this alloy are shown in Figure 4.1 and Figure 4.2 [49]. The segregation existing in this alloy remains a big issue in terms of production and application. The segregation coefficients ($k=Xs/X_L$, where Xs and X_L are the mole fractions of solute in the solid state and liquid in equilibrium at a given temperature) of the main alloying elements in Inconel 718 are listed in Table 4.3 [50] . The interdendritic segregation coefficients of the major elements during solidification have been compiled by Auburtin, as shown in Figure 4.3. Niobium is the most segregated element in this material and its concentration in interdendritic liquid increases as the solidification proceeds. The enrichment of this heavy element results in an increasing value of interdendritic liquid density, from 7.45 g/cm^3 at 1336 ℃ to 7.74 g/cm^3 at 1260 ℃ [50] .Laves phases have a formula of AB_2, where the A atoms are ordered as in diamond, hexagonal diamond, or a related structure, and the B atoms form tetrahedra around the A atoms. In The case of Inconel 718, the formula is $(Ni,Fe,Cr)_2(Nb,Ti,Mo,Si)$.

4.1.2 Nimonic 80A

Nimonic 80A (Nimonic is the registered trademark of Henry Wiggin & Company Ltd., designated as UNS N07080) is a nickel-base precipitation-hardening superalloy. It is one of the alloys used for wrought turbine blades. In recent years, there has been a significant increase in the use of Nimonic 80A in steam-power generating plant. The composition and the heat treatment of the alloy have evolved so as to obtain increasingly high strengths at elevated temperatures. This alloy can be age-hardened by the controlled precipitation of intragranular sub-microscopic γ', which contributes to creep resistance by acting as a barrier to dislocation movement [51].

The melting range of this alloy is 1379 ℃ to 1313 ℃. The various phases present in the final microstructure are: γ', the major strengthening phase, intragranular-occuring primary carbides, nitrides or carbon-nitrides [M(C,N), where M is usually Ti], and B as well as Cr- rich grain boundary carbides of the M_7C_3 and $M_{23}C_6$ types [51] .The data on segregation coefficients of each element for Nimonic 80A are not available. However, an average segregation coefficients of nickel-base superalloys are shown in Table 4.4 [50] . Aluminum and titanium are the major segregated elements during solidification and their segregations into interdendritic region would result in a lighter interdendritic liquid than the bulk.

4.1.3 Waspaloy

Waspaloy (designated as UNS N07001) is a nickel-base, age hardenable superalloy with excellent high-temperature strength and good corrosion resistance. It has good resistance to oxidation at service temperatures up to 560 ℃ for critical rotating applications, and up to 870 ℃ for other less demanding applications. The high-temperature strength of this alloy is derived from its solid solution strengthening elements, molybdenum, cobalt and chromium, and its age hardening elements, aluminum and titanium. Its strength and stability ranges are higher than those typically available for Inconel 718 [52]. In Waspaloy, the γ' phase functions as the hardening phase [53].

The melting range of Waspaloy is 1360 ℃ to 1330 ℃. Its solidification and precipitation sequence is: (1) Proeutectic γ at about 1360 ℃, (2) (γ+ MC) eutectic at about 1240 ℃, (3) precipitation of γ' at about 1045 ℃ [53]. Similar with Nimonic 80A, aluminum and titanium are the major segregating elements. Therefore, the segregation of these two elements into the interdendritic region also results in a lighter interdendritic liquid.

4.1.4 M50

M50 (AISI designation) is derived from a group of high speed steels, with tungsten removed. It has a high hardness after tempering, and wear resistance with good toughness. The steel is widely used in aerospace applications. Its working

temperature lies between 150 ℃ and 300 ℃. The alloying elements used form fine precipitated carbides which increase the mechanical properties during the secondary hardening step [54, 55].

The microstructure of M50 has not been investigated thoroughly in the past. Therefore, the available information on a similar steel M2 is summarized here. The melting range of M2 steel is 1420 ℃ to 1231 ℃. The solidification sequence is listed in Table 4-5. The segregation profiles as well as the variation of the interdendritic liquid density of M2 are shown in Figure 4.4 and Figure 4.5 [50]. Carbides M_6C and MC are found in the equilibrium structure, with M_2C appearing at low LST (local solidification time) values [56]. The presence of M_6C is considered undesirable. It increases the carbide size after heat treatment, which leads to degraded performance in service. Therefore, a low LST is desirable in this alloy in view of suppressing the formation of M_6C. It can be seen from Figure 4.5 that the interdendritc liquid density always increases as the solidification proceeds. Then close to the end of the solidification, the density decreases because the liquid is depleted in carbide forming heavy elements (Mo and W). The segregation coefficients of M2 are not available, yet the data in a tool steel T1 can be used as a reference (Table 4.6) [50].

The solidification sequence of M50 is similar to that of M2 steel, although the transition temperatures are slightly different. Another important difference between these two steels lies in that M50 does not contain tungsten. Due to the existence of

alloying elements Mo, Cr, V in M50 steel, various carbides can be expected in the final microstructures. The composition of the carbides is listed in Table 4.7 [55].

4.2 DS/DSQ Furnace

The equipment used to simulate the interrupted solidification process in remelting is called Directional Solidification and Quenching (DSQ) furnace. Figure 4.6 shows a photograph of the apparatus. A computer controls the rate of removal of the sample from the hot zone containing the alloy sample and a schematic representation of the process is shown in Figure 4.7.

The molten sample having a small diameter as compared with its length was extracted at a controlled withdrawal rate from the furnace. With this arrangement, unidirectional solidification was achieved as the solidification front moved upwards in a closed-end alumina tube. The furnace contains a cylindrical high-density graphite susceptor, which is heated by a high frequency induction device. At this frequency (450 Hz), the induced magnetic field remains confined to the graphite susceptor. Therefore, stirring of the molten material does not take place with eddy currents. Argon gas (98 %) flows through the furnace chamber during melting and withdrawal of the specimen. Quenching is realized by installing a brass tube filled with water below the susceptor.

This steady-state technique of solidification can realize the control on the temperature gradient of the liquid front G as well as the velocity of the growth front R. Therefore, these parameters can be set in order to simulate the practical thermal condition. In addition, the equipment allows the solidifying specimen to be quenched, which makes it possible to observe the development of dendrite microstructure and solute segregation.

Specimens were machined to a diameter of 4 mm and a length of about 60 mm so as to fit inside the alumina containment tubes (outer Φ 6.26 mm). Calibration of the furnace temperature gradient was done with a type-D (Tungsten 3 %Re and Tungsten 25 %Re) thermocouple. A molybdenum specimen, with the thermocouple inserted in it was kept in the hot zone of the graphite susceptor. The temperature gradient was measured as 8.6 ℃/mm near the melting temperature. The cooling rate was about 54 ℃/min at a withdrawal rate of 6 mm/min.

The specimen was held stationary in the furnace hot zone for one hour at a temperature above its melting temperature in order to establish thermal equilibrium. Withdrawal from the hot zone was made through the established temperature gradient using a pre-selected rate. An interruption for a pre-specified time or a reversal to the direction and withdrawal was achieved using computer programs. For example, the following sequence was used in the program "6DSRSDS" and the resulting sample was labeled as "E". The sample was lowered (i.e. directionally solidified) at a speed

of 6 mm/min for 5 mins, the direction of travel reverses (i.e. re-melt) at the same speed for 30 secs, stop for 30 secs, then re-establish directional solidification at 6 mm/min. The "reverse" and "hold" simulate the condition that power is turned back on after a sudden power shut-down. The corresponding process in the real production is explained in Table 4.8. Other labels which have been used to designate the samples are "-EQ", "EWQ", "DS" and "DSQ" and the corresponding processes are listed in Table 4.9.

4.3 Techniques for Characterization

All specimens examined under the optical microscope and the scanning electron microscope were polished down to 1 micron on a diamond lap.

4.3.1 Etching

The materials and the corresponding etchants are listed in Table 4.10.

4.3.2 Optical Microscopy

An optical microscope was used to analyze the bulk dendrite structures as well as the small precipitates. The Optical Microscope used was Nikon Epiphot 300 with CleMEX vision PE^{TM} 3.5.

4.3.3 SEM, EDS and BSE

A Hitachi S-3000N scanning electron microscope (SEM) was used to observe the microstructures using an accelerating voltage of 20 kV. Energy Dispersive

Spectroscopy (EDS) using secondary X-rays was used along with the SEM for analyzing compositions. When using spot as well as area EDS scanning, readings were taken for 100 secs. Backscattered Scanning Electron (BSE) was employed to enhance image contrast due to differences in atomic numbers of the elements.

5. Results

5.1 Inconel 718

5.1.1 Industrial Ingot Containing Banding

An industrial Inconel 718 sample which included tree-ring structures was examined first. Figure 5.1 shows the appearance of the industrial banding (as received from Aubert & Duval Corp, Les Ancizes, France, macroetched). The bands are perpendicular to columnar dendrites and appear lighter than the non-banded regions as indicated in the macrograph. Under a higher magnification, the slightly etched specimen showed that Laves phase and delta phase combinations (Figure 5.2) are orderly distributed along the bands, as shown in Figure 5.3. In order to analyze the compositions of the banded and non-banded regions, only light etching was used. The analyzed area covers a dimension of (200 X 100) μm^2. One measurement of each region was made. The banded region covers those lined up precipitates (A in Figure 5.3). The non-banded region covers the area between two adjacent tree rings (B in Figure 5.3). The acquired data are limited but the results in Table 5.1 show that possibly there is a difference of Nb content between a banded region and the region in between the bands. The errors appearing in the data are the statistical calculation errors and they can show how reliable the results are.

5.1.2 Laboratory Simulation of Banding

Figure 5.4 shows the morphology of the carbides and Laves phase in a directionally solidified Inconel 718 specimen. Strip-like carbides and bulky Laves phases are distributed in this microstructure.

In an attempt to reproduce the tree-ring structure in the laboratory, a number of schemes were designed for simulating the interruption of the solidification process. Those schemes are listed in Table 5.2. A band of structural difference was observed in Inconel 718-E specimen as shown in Figure 5.5. The other schemes did not produce any band.

There is an obvious difference in the etching response of the microstructures within the interrupted region, which can be observed in Figure 5.5. There is no sign of the formation of equiaxial grains during the interrupted region, although this structure is sometimes found in an industrial ingot.

Four distinct zones were observed. They are marked 1 through 4 in Figure 5.5. Zone 1 and zone 4 correspond to normal growth, while zones 2 and 3 represent the interrupted solidification. The microstructures of zone 1, 2 and 3 as seen under a somewhat higher magnification are shown in Figures 5.6, 5.7 and 5.8 respectively. The microstructure in zone 4 was similar to that in zone 1. It can be seen that the directionally solidified dendrite structure does not change during the interruption. The

dendrite spacing, which has been measured, remains similar in each zone, with a value of approximately 100 μm. EDX analysis is used to identify the precipitates and the Laves phase composition is listed in Table 5.3. The microstructures of each zone under a yet higher magnification are shown in Figure 5.9 to Figure 5.11. The observation on this sample clarifies the evolution of the precipitates during the interrupted directional solidification. In the micrograph of the normal growth region, primary and secondary dendrites are seen (Figure 5.6). The interdendritic space contains the primary carbides and the final eutectic carbides as well as Laves phase (Figure 5.9). A closer examination of zone 2 revealed that the primary dendrite spacing remained essentially unchanged, however, the secondary arms became almost entirely dissolved. The types of precipitates found in the region between the primary dendrites remain unchanged. However, the morphology of these precipitates changed.

The microstructures seen under a yet higher magnification are shown in Figures 5.9 to 5.11. From the micrographs it is seen that the average amount of precipitates in zone 2 (Figure 5.10) is less than in zone 1 (Figure 5.9). The Laves phase and the carbide precipitates had dissolved. Semi-quantitative analyses have been done by counting the quantities of different precipitates under the same magnification. In zone 3, there were more precipitates and they were elongated along the liquid channel. The size of Laves phase existing in zone 3 was found to be bigger than in zone 1. In addition, the relative proportion of Laves phase to the carbides was higher in zone 3 as compared with that in zone 1.

In order to understand the mechanism responsible for the formation of the precipitates during the holding process, quenching experiments were conducted on Inconel 718. The micrographs have been taken in the zone 2 of the quenched specimens as shown schematically in Figure 5.12. The resulting microstructures are shown in Figures 5.13 and 5.14. The micrographs shown in Figure 5.13 and Figure 5.14 were taken on specimens having undergone EQ treatment (Directional solidified, reverse, hold and quench) and EWQ treatment (Directional solidified, reverse and quench) respectively (Table 4.9). Structures all include carbides and laves phase. It is clear that the carbides and Laves phase mainly precipitated from the liquid channels which existed in this region. The script-like carbides in the sample having a hold period (Figure 5.13) are larger and greater in quantity than on the specimen without holding (Figure 5.14).

Compositional analysis has been done on the Inconel 718-E specimen using EDS technique by analyzing areas along the solidification direction. Each scanning area had a size of (400 X 200) μm^2 (shown in Figure 5.5) which covers the width of at lease 4 dendrites. One measurement was made at each location. Figure 5.15 is the plot of the bulk Nb content versus distance along the specimen axis. No significant changes in the composition of the primary element which segregates (Nb) can be observed.

It may be noted that δ phase precipitates were observed in the microstructure of the industrial Inconel 718 specimen (Figure 5.2). However, such precipitates were not observed in the banded zone on the Inconel 718-E (Figures 5.9 to 5.11). In order to see if δ phase can be precipitated through a longer exposure to a lower temperature, heat treatment was given to the Inconel 718-E specimen at 870 ℃ for 24 hrs. The specimen was cooled in the air. The microstructure of the heat treated specimen is shown in Figure 5.16. Precipitations of the δ phase occurs as a result if the longer exposure to the lower temperature. This microstructure is similar to that observed on the industrial Inconel 718 specimen containing the tree rings (Figure 5.2).

5.2 Nimonic 80A and Waspaloy

Results of an industrial Waspaloy are presented below. No industrial Nimonic 80A ingot was analyzed.

5.2.1 Industrial Ingot Containing Banding

Figure 5.17 shows the industrial banding of Waspaloy (forged, as received from Mitsubishi). The carbide precipitates which are distributed within the banded region are shown in Figure 5.18. Figure 5.19 is the image of the region outside the band, showing no big precipitates. The compositional analysis was done in a way similar to that done for the industrial Inconel 718 specimen. The original data are listed in Table 5.4. The numerical averages of the original data are listed in Table 5.5. The result

shows no significant difference in the element contents (especially Ti) between banded and non-banded regions.

5.2.2 Laboratory Simulation of Banding

The microstructural responses of Nimonic 80A and Waspaloy to the interruption were found to be similar. Therefore, the results are presented together. The interruptions (reverse, hold, directional solidified) were made in a manner identical to that of Inconel 718-E. Figures 5.20 to 5.22 show the microstructures as observed on Nimonic 80A-E specimen. Microstructures seen on the Waspaloy-E specimen are shown in Figures 5.23 to 5.25. The primary dendrite spacing as measured is approximately 100 μm. Nimonic 80A-E sample did not show a faint band upon etching. However, Waspaloy-E showed a small band upon etching. As for microstructure, like Inconel 718-E, similar general microstructual evolution was observed in the interrupted region. However, differences were found in the appearance of precipitates, as described in the following.

In Figure 5.20 to Figure 5.22, a change in the structure of the precipitates (gamma prime) is seen. Based on these differences, this sample has been divided into three zones, i.e. zone 1 (normal growth), zone 2(corresponding to zone 2 in Inconel 718-E, where the decreased size of precipitates is observed) and zone 3(the enlongated precipitates are observed). The gamma prime phase appeared as small, needle-like precipitates in the normal growth region (zone 1). While in the interrupted

region, the size of the gamma prime became even smaller in zone 2. Elongated and aligned precipitates were observed in the interdendrtic channels in zone 3. Similar observations were made with the microstructure on Waspaloy (Figure 5.23 to 5.25).

The EDX analysis was also done for Nimonic 80A-E. Similar to the analysis on Inconel 718-E,one measurement was made at each location. Again, the compositional analysis (Figure 5.26) does not indicate any obvious change in the concentration of Ti, the principal element segregating into the liquid during solidification. The results of the 4-zone compositional analysis on Waspaloy-E are listed in Table 5.6. No significant change was observed.

5.3 M50 Steel

An industrial ingot was not available. Only the results obtained in the laboratory are presented.

Interruption of the solidification sequence in the laboratory was similar to that carried out for Inconel 718-E. No band was observed on macro-etching. However, an examination of the microstructures along the length of the specimen showed differences as illustrated in Figure 5.27. From EDX analysis, MC and M_2C were identified as the main carbides formed in the laboratory solidification process and their morphologies are shown in Figure 5.28. M50-E sample is divided into three

zones according to the relative proportion of MC/M_2C as shown in Figures 5.28 to 5.30. It has been found that zone 1 is dominated by MC with a small amount of M_2C, while in zone 2, more M_2C carbides show up. In the last zone, the amount of M_2C decreased to about the same extent as in zone 1.

The bulk compositional analysis with an area of (1000 X 500) μm^2 is shown in Figure 5.31. One measurement was made at each location. It indicates that the composition of vanadium varied with length along the direction of solidification. From left to right, the bulk compositional analysis started form the bottom to the top of the sample M50-E. Due to the larger Liquid –Solid temperature difference of M50 relative to superalloys noted earlier, the EDS analysis required covering a greater distance along the specimen axis. Starting from the bottom of the specimen, the composition of vanadium decreases somewhat upon entry into the interrupted region. The decrease of vanadium composition remains until it reaches about 18 mm. After 20 mm the vanadium concentration is restored to that of the bulk material. Possibly a region which has a higher vanadium concentration than that of the bulk material exists between 18 mm and 20 mm(indicated by the arrow in Figure 5.30). A concentration variation in carbon may also exist. However, carbon concentration could not be measured with EDX.

6. Discussion

6.1 Banding in Industrial Ingots

Examination of the industrial Inconel 718 ingot carried out in the present work shows that large precipitates exist within the bands (Figure 5.2). Moreover, a composition difference was found between banded and non-banded regions in respect of Nb content (Table 5.1). This difference, although small, is significant from an industrial perspective. For Nb contents greater than 5.3 wt%, the homogenization treatment needed to eliminate Laves phase is not feasible.

The measured composition difference could result from the liquid metal movement caused by electromagnetic and buoyancy forces in the ingot liquid pool. Momentum transfer between the bulk liquid and the mushy zone would then cause segregated liquid to flow through the dendrite network and collect in larger volumes than the original interdendritic spaces. A locally higher Nb content, formed by this mechanism has been postulated for the initial stage of freckle formation [57]. There is general agreement in the literature that the above mechanism represents the initiation stage of freckle formation in this type of alloy in spite of the fact that model simulations of the remelting processes consistently show little or no liquid circulation at the liquidus line. One example of such work applied to the ESR process is shown in Figures 6.1 and Figure 6.2 [58]. It is seen from the figures that the velocity of the fluid flow in front of the liquidus line reaches zero, indicating the absence of fluid flow at

this location. However, in the present work an actual difference in local composition has been measured (Table 5.1). It is difficult to account for this observation by any other mechanism than the above and so it is suggested that in industrial Inconel 718, fluid flow in front of the liquidus line must have taken place. The observation made in the present work is hence not consistent with the prediction of the models. It is to be noted that the models assume an axisymmetric 2-D steady state condition for the flow computation. One reason for the discrepancy noted above could be that instability in the process temporarily upsets the assumed axisymmetric force distribution and hence could generate a local flow not predicted in the steady state.

Observation of the delta-phase formed in the heat-treated Inconel 718-E specimen (Figure 5.16), which has a similar thermal history to the industrial 718 ingot (Figure 5.2), suggests that the low cooling rate of the industrial "as-cast" Inconel 718 sample is responsible for the observed microstructural difference between these cases and the as-cast laboratory samples. This inevitable low cooling rate of a large ingot thus produces a form of heat treatment even when the nominal condition is "as-cast".

Unlike industrial 718, the industrial Waspaloy ingot showed no composition difference between banded and non-banded regions (Table 5.3). It can be concluded from this observation that the compositional difference does not necessarily exist in any banded structure and the existence of this difference is determined by the alloy type and the process parameters. A difference in microstructures between the banded

and non-banded region was found in the industrial Waspaloy specimen. The carbide precipitates which were found within the banded region (Figure 5.18) did not exist outside the band (Figure 5.19). This finding agrees with the results acquired from the laboratory-produced Waspaloy-E specimen (no composition change, but the change of precipitates).

6.2 Banding in the Laboratory Simulation

For superalloys, based on the data of the temperature and cooling rate during the ESR and VAR processes (Figure 2.7 and Figure 2.8), we simulated the solidification of the mid-radius region of a typical industrial ingot. According to the experimental and modeling results shown in Figure 2.9 and Figure 2.10, our laboratory conditions, a temperature gradient of 8.6 ℃/mm and a cooling rate of 54 ℃/min, would result in a columnar dendrite structure (Figure 2.10) with a primary dendrite spacing of approximately 100 μm(Figure 2.9). This was found to be the case in the laboratory simulation (Section 5.1.2).

According to Kurtz's [59] diagram on single phase solidification morphologies as shown in Figure 6.3, our experimental conditions would result in equiaxed dendrites (designated by the arrow), which is different from the results according to Fernihough's morphology diagram in Figure 2.10 [42] . As Fernihough's diagram predicted, the real solidification morphology is columnar dendrite. Therefore, Kurtz's diagram is not reliable enough to estimate the solidification morphology.

According to the present results from each material (Inconel 718, Nimonic 80A, Waspaloy, M50), it is found that the difference between the banded area and the non-banded area in the laboratory simulation lies in the appearance of precipitates corresponding to different solidification conditions. The variation in Laves phase size due to the interruption in solidification (Inconel 718-E, Figures 5.9 to 5.11) can be explained as follows. The interruption gave the solidified structures in zone 2 (Figure 5.10). The observed zone 2 was completely solidified before remelting occurred. During the interruption, this region did not undergo melting, but was maintained at a high temperature in the solid state. That high temperature exposure resulted in a modification of the structure in which the Laves phase precipitates became smaller in size. In contrast, zone 3 (Figure 5.11) was partly solidified before the remelting took place. The lowering of cooling rate during solidification gave increased segregation as expected, thus giving the Laves phase formers, such as Nb, Cr, Ni, enough time to collect locally. As noted in Section 5.1.2 the increased proportion of Laves phase relative to carbides in zone 3 is consistent with this explanation. The greater amount of carbides in Inconel 718-EQ (Figure 5.13) than Inconel 718-EWQ (Figure 5.14) indicates that the holding period enhances the nucleation and growth of carbides. The same hypothesis can be applied to explain the variation of γ' phase in Nimonic 80A-E as well as in Waspaloy-E. In the case of M50 steel, the change of the ratio of MC/M_2C (Figures 5.28 and 5.29) occurred during the interrupted solidification, with a lower value of MC/M_2C in the interrupted region. This effect is partly due to the

method of counting the M_2C particles metallographically. MC precipitates at a higher temperature than does M_2C [56] and MC is precipitated at a liquid fraction of at least 0.6. Therefore, the interrupted process does not substantially affect the quantity or size distribution of MC. In the normal solidification region, most M_2C is of a small size (small LST value). During the remelting, the secondary arms dissolved thus the eutectic volume became larger than during normal growth. Therefore, M_2C precipitates became numerous and larger than in the normal growth region thus helping to decrease the measured MC/M_2C ratio based on particle counting.

No compositional difference between normal growth and interrupted regions were observed in the three superalloys examined in the present work (Figure 5.15, Figure 5.26 and Table 5.3). This finding is to be expected in the case of Inconel 718 because the density of the segregated liquid in this material is heavier than in the bulk liquid due to the segregation of Nb. Therefore, during solidification, the interdendritic liquid would remain in the interdendritic region thus not causing thermosolutal convection flow. However, in the case of Nimonic 80A and Waspaloy, due to the segregation of aluminum and titanium, the interdendritic liquid should become lighter than the bulk liquid. In the accepted freckle formation theory [57], the creation of a liquid of a lower density below that of a heavier liquid would set up thermosolutal convection due to the density difference. In the configuration used in the present experiments, the dendrite network is formed in a vertical direction and so if there was significant upward flow of interdendritic liquid during the interruption, the alloy

should have shown corresponding observable differences in bulk composition when the sample was analyzed in the vertical direction i.e. along the sample axis. Such a difference was not observed. Based on the results from compositional analysis on Nimonic 80A (Figure 5.26), it is postulated that the reason for the absence of such flow arises in the relatively small interdendritic spacing. According to Wang's [60] work on freckle formation mechanism of Nimonic 80A, freckling occurs at a freezing rate of 0.05 ℃/s, but not at 0.3 ℃/s. The first cooling rate results in a primary dendrite spacing of about 200/250 μm, the second is 110 μm. The primary dendrite spacing in our research is in the range of 100 μm which is not sufficient to permit the fluid flow according to the theory. Because of the value of k_{Al} and k_{Ti} [50] (0.92, 0.69), the main segregating elements in Nimonic 80A and Waspaloy would not cause severe segregations. Therefore, the flow would not develop easily in the above two alloys. For M50 steel, the vanadium composition near the top of the sample (at 18 mm, the composition peak) is higher than in the interrupted region (Figure 5.31), which suggests bulk convection flow from the solidifying region driven by the lower density due to vanadium segregation of the interrupted region. The rejection of vanadium from the interrupted region also results in more M_2C carbides (poor in V) and less MC carbides (rich in V) in this region.

A model has been proposed by Yang *et al* [61] to simulate the formation of the stray grains during the single crystal casting of a nickel-base alloy. The melt-back process during which the stray grains are often found in single crystal castings is

similar to the interrupted solidification process that has been discussed in the current research. The predicted microstructure during the melt-back of a single crystal seed under a condition of flat isotherms is shown in Figure 6-4. An initial steady-state microstructure was produced by simulating for 40 s at a constant pulling velocity. The melt-back process was then simulated by moving the isotherms downward by 2.25 mm, raising the temperature around the tips of the primaries above their liquidus. The seed was then held at this temperature for 10 sec. During melt-back, the sharp curvature of the stems where the secondaries are attached to the primaries melts before the secondaries themselves, pinching them off from the primaries. And the cores of primaries are the last to melt. The melt back and pinch-off secondary arms and their subsequent rotation due to the local fluid flow altered the crystallographic orientation, resulting in the random stray grains. As the mold withdrawal begins again, the primaries and pinched-off secondaries ripen and grow. This simulation given by Yang explains the reason for the existence of stray grains during the melt-back process and could possibly also account for the equiaxed grains frequently found in the banding of industrial ingots.

In an industrial process, the fluid flow which is caused by electromagnetic force and buoyancy force has two effects. First, it causes fluctuations in the thermal field. This fluctuation results in the supercooling at the solidification front thus enhancing the possibility of the occurrence of equiaxed grains. Moreover, this flow encourages the break-off of secondary arms. The broken arms having undergone a change in

orientation as a result of the flow become sites for the nucleation of equiaxed grains. In the lab simulation made in the present work, no equiaxed grains were observed. This finding has two possible explanations. One possibility is that the thermal field during the experiment was stable due to the absence of fluid flow. Because of the small size of the sample and the absence of magnetic stirring, it is unlikely that the fluid flow will exist during the unidirectional solidification. Another explanation may be that the secondary dendrites were completely remelted during the interruption thus being unable to provide the nucleation site.

6.3 Comparison of Industrial and Lab-simulated Banding

The laboratory-produced banded structures are different from those in the industrial ingots. One of the differences lies in the composition variation of the main segregating elements which was found in the industrial Inconel 718 but not in the lab-produced specimens. Another difference lies in the precipitates which are the main characteristic used to identify banded structures. In the lab-produced banded Incone 718 sample, only the morphology change of Laves phase can be observed (Inconel 718-E, Figures 5.9 to 5.11). However, in the industrial Inconel 718 sample, the big Laves phase precipitates were present within the band but absent outside the band (Figure 5.3). For lab-produced Waspaloy, the change in the morphology of the gamma prime phase is the main feature to identify the banded region (Figures 5.23 to 5.25). Whereas, for industrial sample, the existence of carbide precipitates was found within the band but not outside the band (Figure 5.18, Figure 5.19). This finding

indicates the following points. The compositional difference, in other words, segregation does not necessarily exist in the banded structure. Instead, the microstructure variation in precipitates is the essential feature of the banding. The different characteristics of the banded structures between the industrial and the lab-produced samples is probably due to the more complicated processing and heat treatment during the real industrial production.

7. Conclusion

There are several conclusions which can be made based on the present research work having been done.

1. The compositional variations observed in the banded region of the industrial ingot of Inconel 718 were not observed in the interrupted region of any of the directional solidified samples examined. It is to be concluded that these features arise in the industrial ingot due to the momentum transfer from the bulk liquid to the interdendritic zone during the event which produces the banding.

2. The compositional variations measured in the industrial ingot of Inconel 718 indicate movement of the interdendritic liquid to form collections of segregated liquid which can subsequently be the initiation point for freckle formation. The remelting of secondary dendrites which was observed in the interrupted region of the DS possibly changes the permeability of the dendrite mesh.

3. The response of Inconel 718 to interrupted solidification shows primarily in the morphology and distribution of primary precipitates. The primary carbides are enlarged and since the eutectic pool size is increased, the eutectic carbides and Laves phase particles are also enlarged. Due to removal of the secondary dendrite arms, the

eutectic regions are elongated in the primary solidification direction. These effects are to be anticipated due to the holding time in the high temperature region.

4. Similar effects to those described above were found in Nimonic 80A and in Waspaloy. In these alloys, the affected precipitates are primary gamma prime, which do not appear to change subsequently in size, but which are aligned in the same manner as that described above.

5. M50 steel shows some differing characteristics to the superalloys. The variation in vanadium composition in this steel proved the existence of interdendritic fluid flow during the interruption, thus resulting in the variation of the MC/M_2C ratio.

6. The interruption in solidification condition during a directionally solidification itself can produce banding. The compositional difference is not necessarily required to form the banded structure. Instead, the microstructure variation in precipitates is the essential feature of the banding. The different characteristics of the banded structures between the industrial and the lab-produced samples is probably due to the more complicated processing and heat treatment during the real industrial production.

7. The effect of interrupted solidification on mechanical behavior is beyond the scope of this work. However, it is clear that the changes described above would influence the materials properties in the interrupted regions. The extent to which the

properties would be affected is clearly dependent on the severity of the interruption and on the alloy grade.

Tables

Table 4.1 Nominal composition of original materials (wt%)

Alloy/element	C	Cr	Co	Mo	Nb	Al	Ti	Zr	Mn	B	Fe	Ni
Inconel 718	0.04	18.5	-	3.0	5.1	0.5	0.9	-	-	-	18.5	bal
Nimonic 80A	0.05	19.5	1.0	-	-	1.4	2.25	-	-	-	1.5	bal
Waspaloy	0.06	19.0	12.3	3.8	-	1.2	3.0	0.01	0.45	0.005	-	bal

Steel/element	C	Cr	Co	Cu	Mn	Mo	Ni	P	Si	S	W	V	Fe
M50	0.85	4.25	0.25	0.1	0.35	4.5	0.15	0.015	0.25	0.015	0.25	1.1	bal

Table 4.2 Major phases and reactions in Inconel 718 [45, 46]

Temperature(℃)	Reaction	Phase formula
1336	L→γ	Austenite matrix
1290	L→γ+MC	(Ti,Nb)C
1175	γ→Laves phase	$(Ni,Fe,Cr)_2(Nb,Ti,Mo,Si)$
1145	γ→δ	Ni_3Nb
1000	γ→γ''	Ni_3Nb
1000	γ→γ'	Ni_3Al, $Ni_3(Al,Ti)$

Table 4.3 Segregation coefficients of various elements in Inconel 718 [50]

Element	Al	Co	Cr	Fe	Mo	Nb	Ti
k	1.08	1.05	1.06	1.1	0.99	0.44	0.59

Table 4.4 Average segregation coefficients of various elements in nickel-base superalloys [50]

Element	Cr	Co	Al	Ti	Fe
k	1.02	1.07	0.92	0.69	1.06

Table 4.5 Solidification sequence of M2 steel [50,56]

Transformation temperature (℃)	Reaction
1440	Liquid→δ ferrite
1420	Liquid+ferrite→austenite
1260	Liquid→MC
1242	Liquid→austenite + M_6C
1236	Liquid→austenite + M_2C

Table 4.6 The segregation coefficient of the major segregating elements in T1 tool steel [50]

Alloy	Cr	Mn	V	W
k	0.87	1.38	0.61	0.78

Table 4.7 Averaged analytical results of the elements content in the carbides in M50 (at%) [55]

Carbide/element	Fe	Cr	Mo	V
M_6C	35	7	56	2
M_2C	3	13	69	15
MC	1	6	40	53

Table 4.8 Interruption during the laboratory experiment and that occurring during production

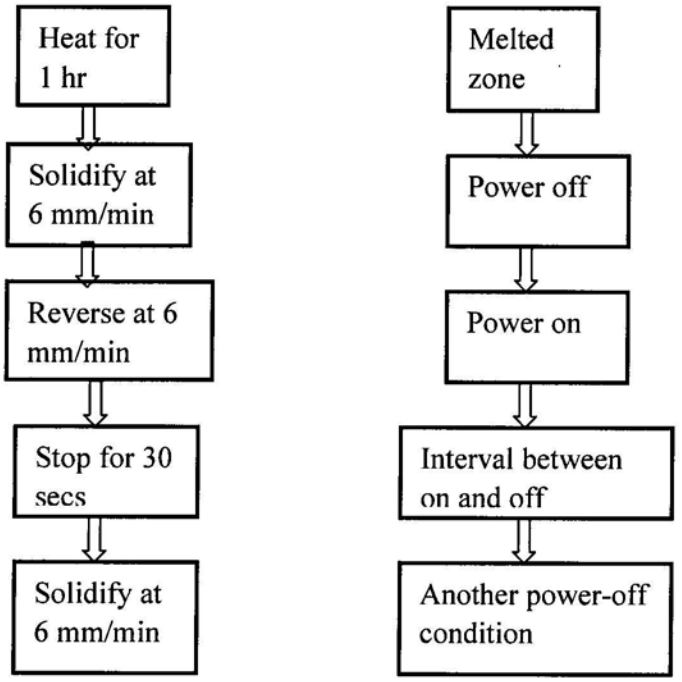

Table 4.9 Designations used for various sequences

Label	Process
E	DS* at 6 mm/min for 5 mins→reverse(30 secs)→stop(30 secs)→DS(same speed)
EQ	DS at 6 mm/min for 5 mins→reverse(30 secs)→stop(30 secs)→Quench
EWQ	DS at 6 mm/min for 5 mins→reverse(30 secs)→Quench
DS	DS at 6 mm/min
DSQ	DS at 6 mm/min→Quench

* DS stands for Directional Solidification.

Table 4.10 Etchants used during specimen preparation

Material	Inconel 718	Nimonic 80A	Waspaloy	M50
Etchant	Marble's*	Marble's	Marble's	**

* Marble's: 4 g $CuSO_4$, 20 ml HCl, 20 ml H_2O

** 4 g NaOH, 10 g $KMnO_4$, 85 ml H_2O

Table 5.1 Concentration of principle segregating elements within and outside the banded region in industrial Inconel 718 (wt%)

Area/element	Al	Fe	Cr	Mo	Ti	Nb
Banded region	0.52±0.07	17.21±0.23	17.09±0.19	2.24±0.12	0.99±0.08	5.63±0.14
Non-banded	0.48±0.07	17.57±0.23	17.24±0.19	2.38±0.12	0.87±0.07	5.29±0.14

Table 5.2 Schemes used in the laboratory to simulate banding

Designation of specimen	Description of program
Inconel 718-A	6 mm/min DS to the end
Inconel 718-B	6 mm/min for 4 cm, stop 1 min, 6 mm/min to the end
Inconel 718-C	6 mm/min for 4 cm, reverse at 6 mm/min for 30 secs, 6 mm/min to the end
Inconel 718-D	6 mm/min for 4 cm, increase to 12 mm/min to the end
Inconel 718-E	6 mm/min for 4 cm, reverse at 6 mm/min for 30 secs, stop 30 secs, 6 mm/min to the end

Table 5.3 The composition of Laves phase found in Inconel 718-E specimen (at%)

Element	Al	Si	Ti	Cr	Fe	Ni	Nb
Content	0.46±0.16	1.78±0.15	1.12±0.11	16.62±0.23	12.74±0.23	47.19±0.46	20.09±0.15

Table 5.4 Measured concentration of the segregating elements within and outside the banded region for industrial Waspaloy(wt%)

Region/element	Al	Ti	Cr	Co	Mo
Banded region	1.00±0.06	2.91±0.07	19.30±0.15	13.680±0.18	3.21±0.08
	0.94±0.06	2.98±0.07	19.51±0.15	13.67±0.18	3.16±0.08
Non-banded region	0.94±0.06	2.98±0.07	19.52±0.15	13.67±0.18	3.15±0.08
	0.98±0.06	2.93±0.07	19.45±0.15	13.69±0.18	3.20±0.08
	0.98±0.06	2.97±0.07	19.40±0.15	13.67±0.18	3.16±0.08

Table 5.5 The average segregating element content within and outside the banded region for industrial Waspaloy(wt%)

Area/element	Al	Ti	Cr	Co	Mo
Banded region	0.97±0.06	2.94±0.07	19.40±0.15	13.68±0.18	3.18±0.08
Non-banded region	0.97±0.06	2.96±0.07	19.46±0.15	13.67±0.18	3.17±0.08

The data listed in this table are the numerical average of the data in Table 5.4.

Table 5.6 The segregating element contents in the four zones of Waspaloy-E specimen (wt%)

Zone/element	Al	Ti	Cr	Co	Mo
Zone 1	1.49±0.07	2.93±0.09	19.36±0.17	13.20±0.19	3.88±0.09
Zone 2	1.59±0.07	3.04±0.09	19.40±0.17	13.32±0.19	3.84±0.09
Zone 3	1.48±0.07	3.18±0.09	19.6±0.17	12.94±0.19	3.89±0.09
Zone 4	1.52±0.07	3.01±0.09	19.33±0.17	13.42±0.19	3.98±0.09

Figures

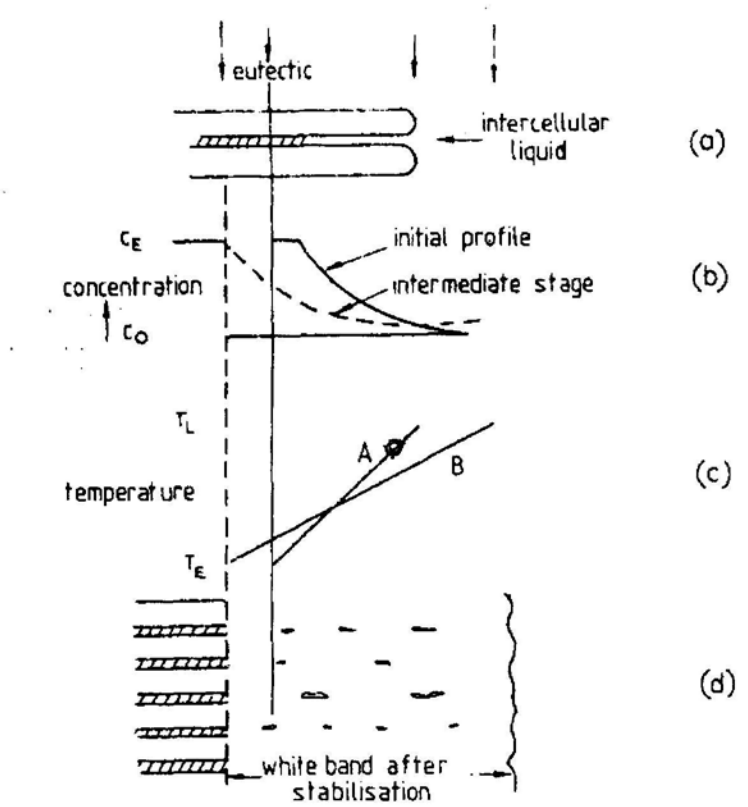

Figure 2.1 Beech's banding formation theory. (C_E is eutectic concentration, C_0 is alloy composition, T_E is eutectic temperature, T_L is liquidus temperature)

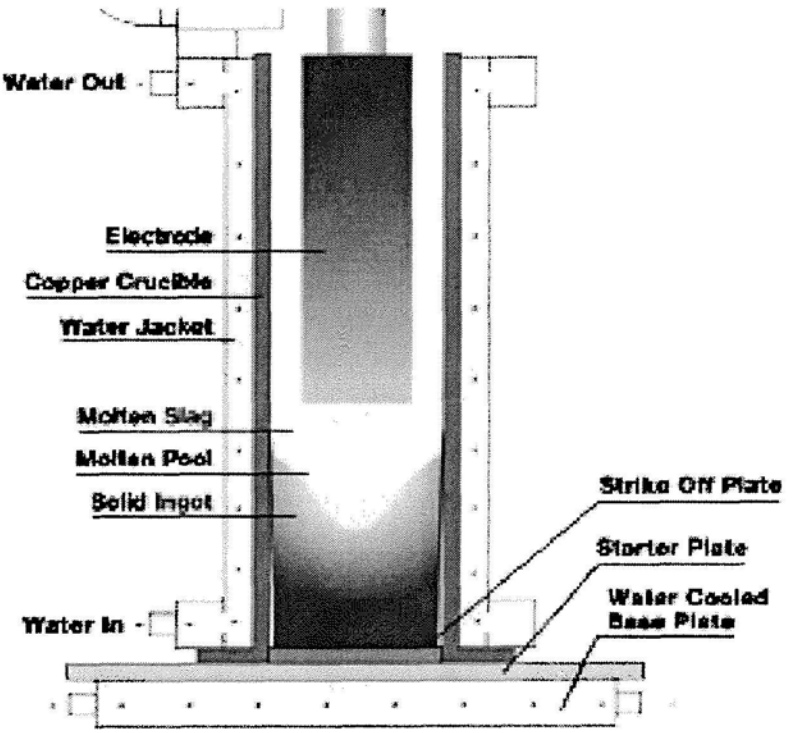

Figure 2.2 Description on ESR process

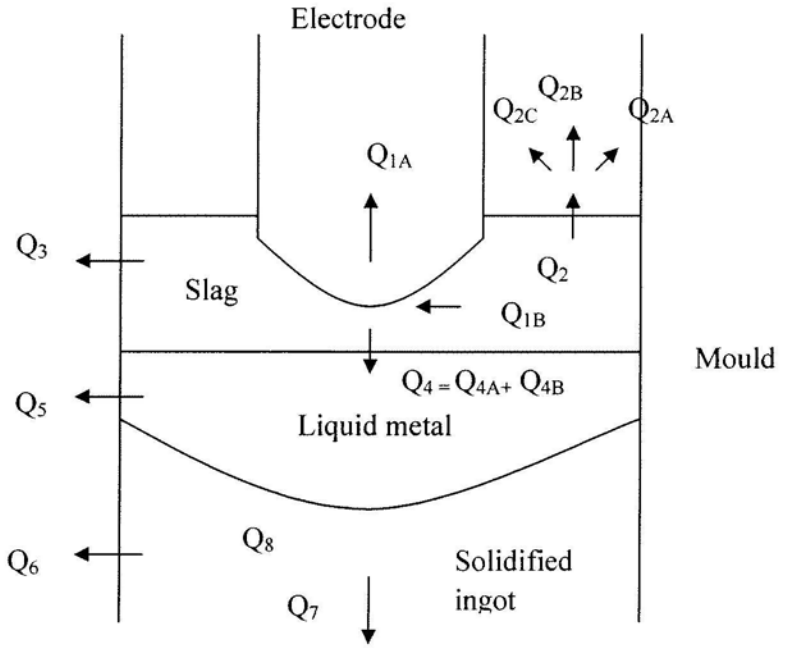

Figure 2.3 Heat flow in ESR process [32]

Q_{1A}, heat required to melt the electrode,

Q_{1B}, heat required to superheat the liquid metal drops,

Q_2, heat lost by radiation from the slag surface to mold cooling water, gases and electrode,

Q_3, hat lost to mould cooling water across the slag bed,

Q_{4A}, heat transferred across slag/metal interface as sensible heat of the falling metal drops,

Q_{4B}, heat transferred across slag/metal interface by convective heat transfer,

Q_5, heat loss to mould cooling water across the liquid metal pool,

Q_6, heat loss to mould cooling water across the solidified ingot,

Q_7, heat lost to base plate cooling water,

Q_8, sensible heat retained by the solidified ingot.

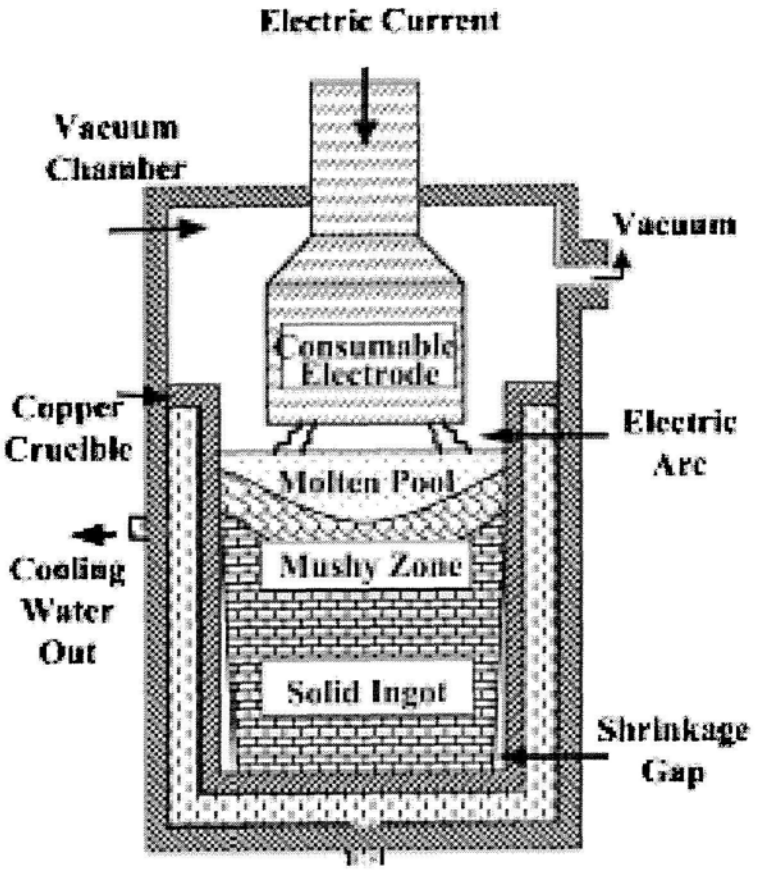

Figure 2-3 Description on VAR system [4]

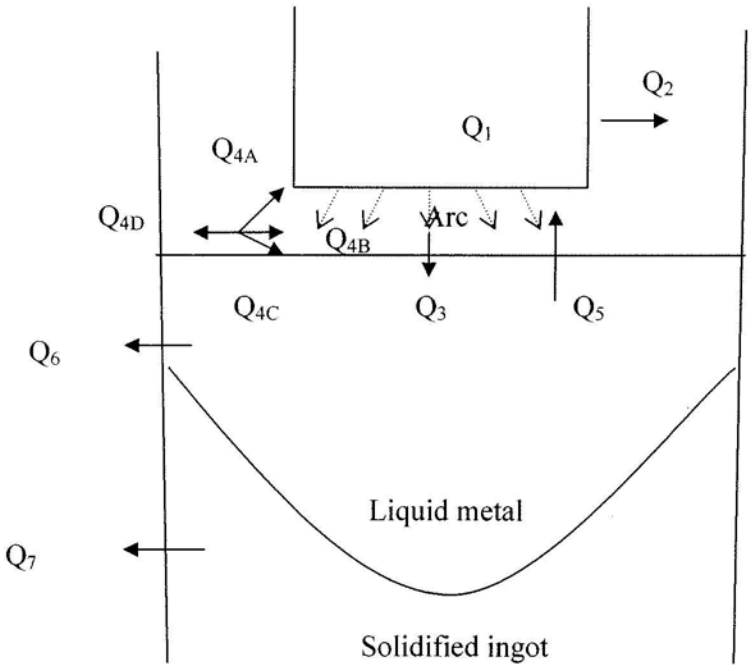

Figure 2.5 Heat flow during VAR process [35]

Q_1, net power supplied at melting tip of electrode,

Q_2, heat lost by radiation from electron to mould,

Q_3, heat transferred due to the falling metal droplets,

Q_{4A}, heat supplied by arc to superheat the liquid metal droplets,

Q_{4B}, heat supplied by arc to electrode,

Q_{4C}, heat supplied by arc to ingot,

Q_{4D}, heat loss from the arc to the mould,

Q_5, heat radiated by ingot to electrode tip,

Q_6, heat lost to the mould across liquid metal pool,

Q_7, heat lost to the mould across the solidified ingot.

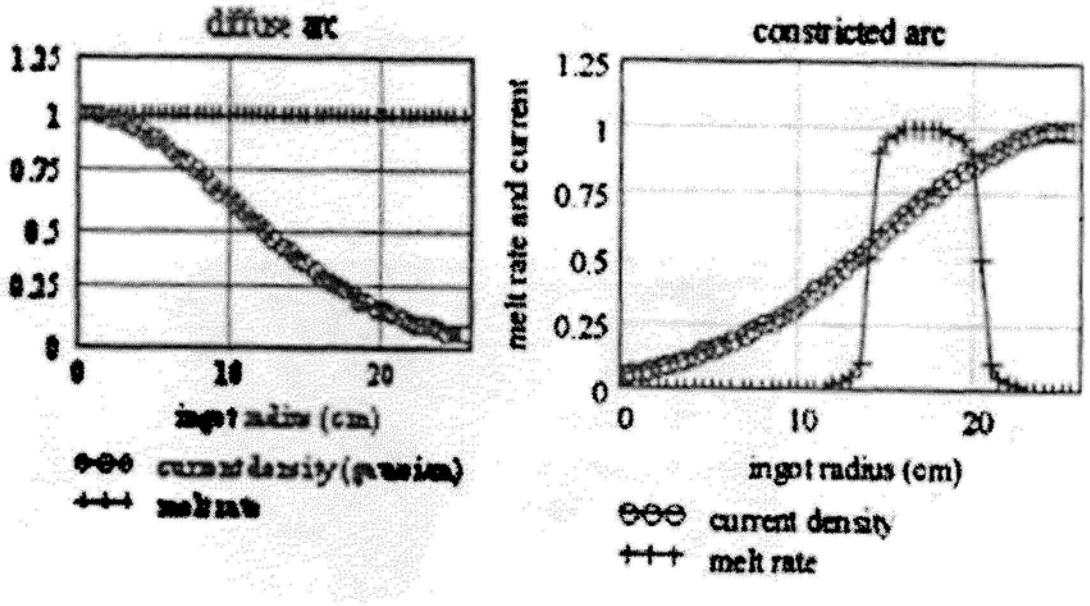

Figure 2.6 Metal and current injection on the surface of the pool; the left plot is for a diffuse arc and the right plot is for a constricted arc

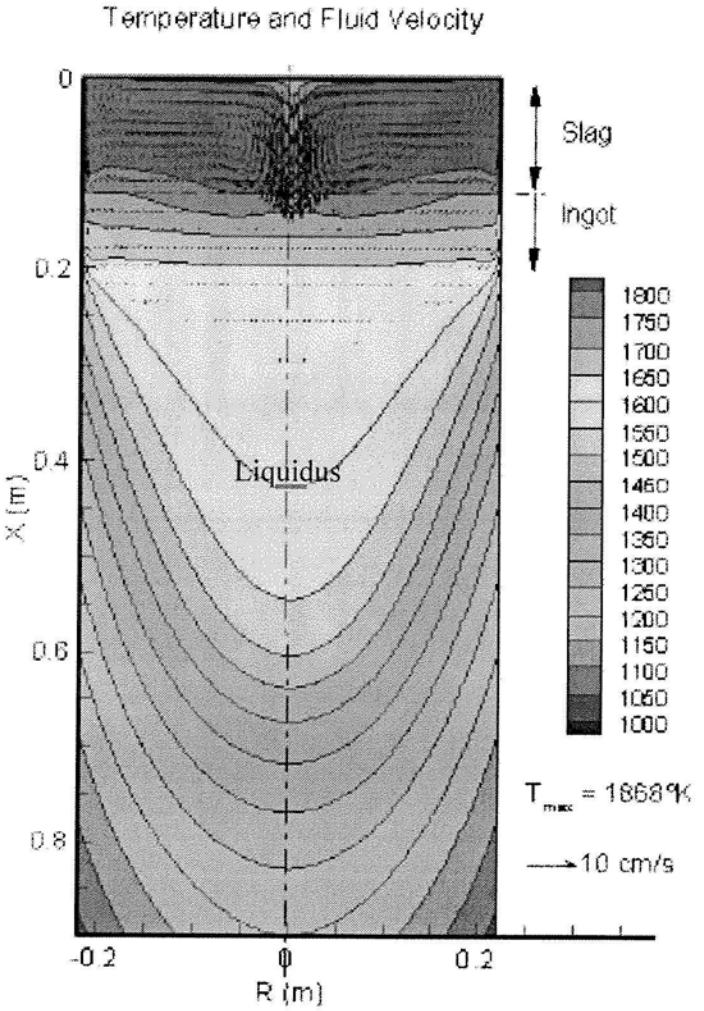

Figure 2.7 Fluid velocity and temperature field for alloy Inconel 718

(Slag Height=120mm,Electrode Diameter=339mm, Ingot Diameter=440mm, Total current=13.5kAmp, AC Frequency=60Hz,Power=360KW, Melt rate=6.75kg/min)

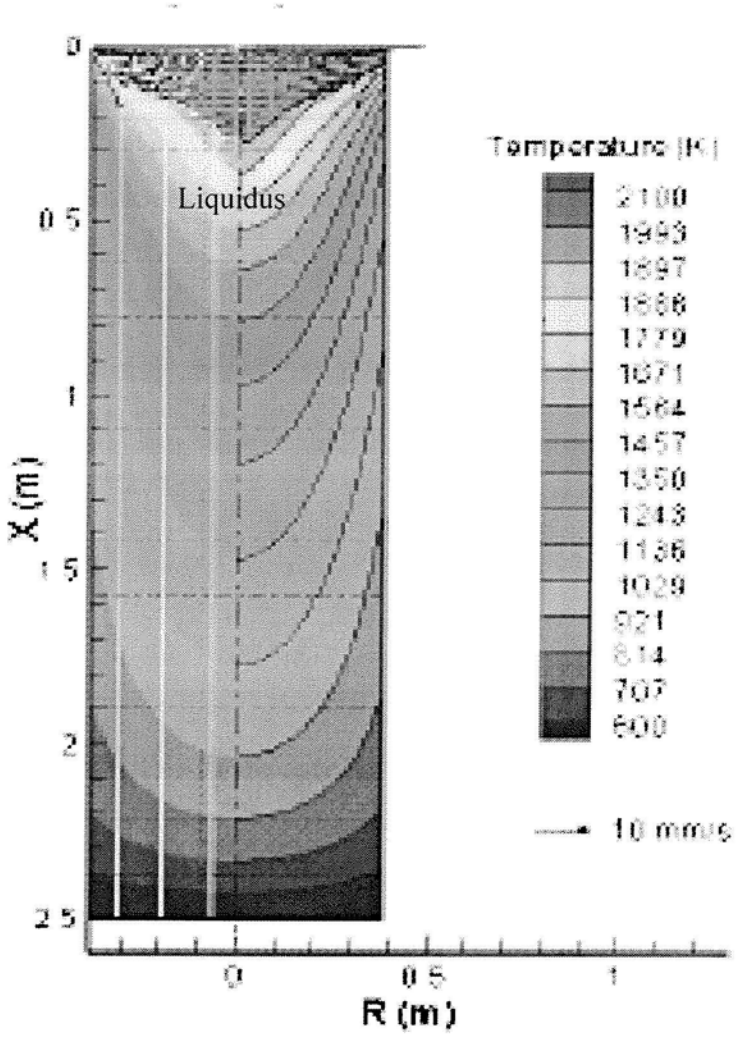

Figure 2.8 Temperature distribution during a practical VAR process for Ti-64 alloy (Ingot diameter=760mm, Electrode diameter=660mm)

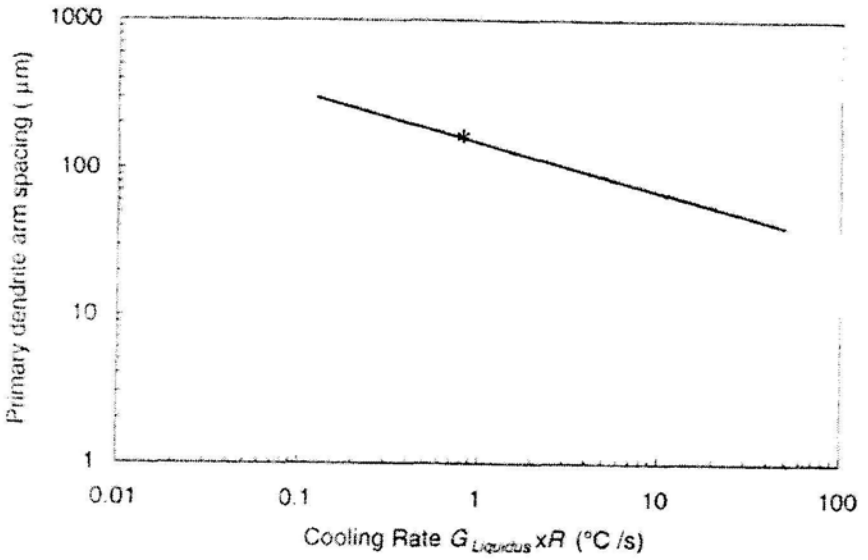

Figure 2.9 Variation of primary dendrite arm spacing with cooling rate

(Asterisk shows the position in the present DS experiment)

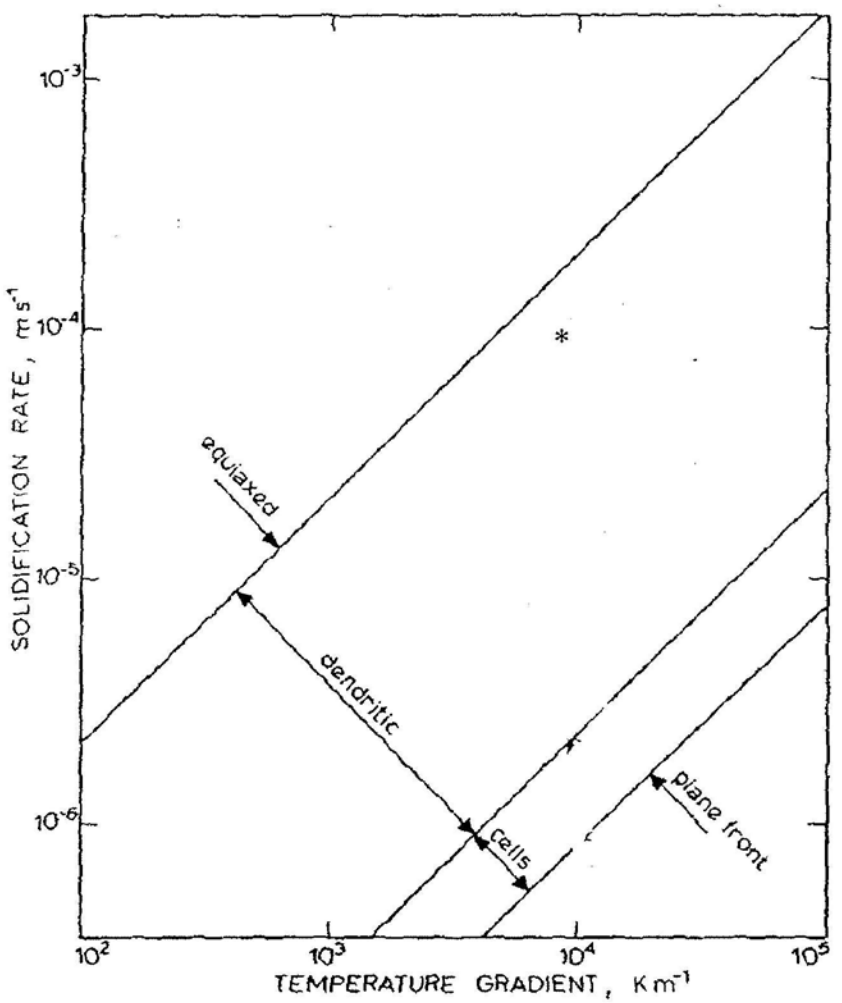

Figure 2.10 Morphologies of Directionally solidified Nickel based superalloys

(Asterisk shows the position in the present DS experiment)

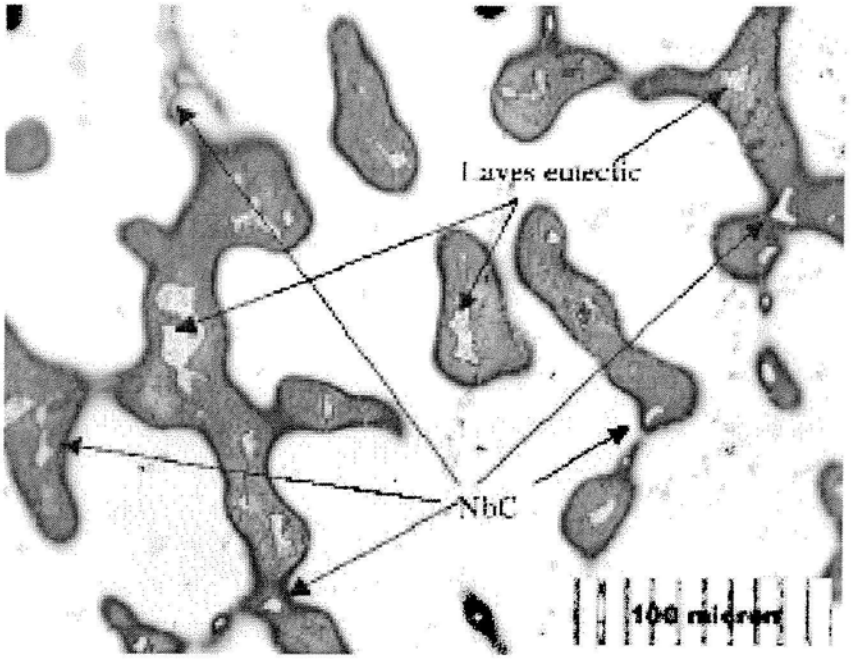

Figure 4.1 Laves phase and carbides of a directional solidified Inconel 718 sample [49]

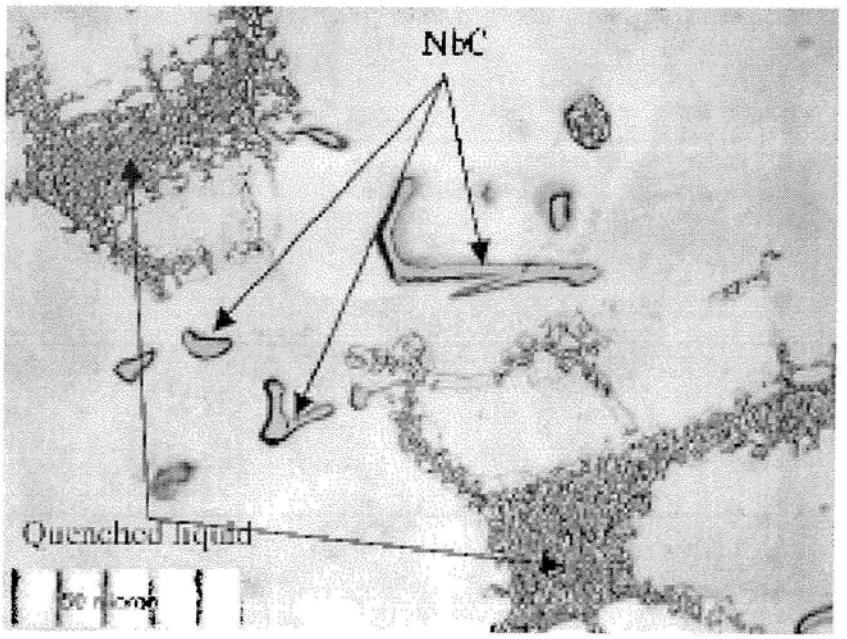

Figure 4.2 Carbides in a directional solidified and quenched Inconel 718 sample [49]

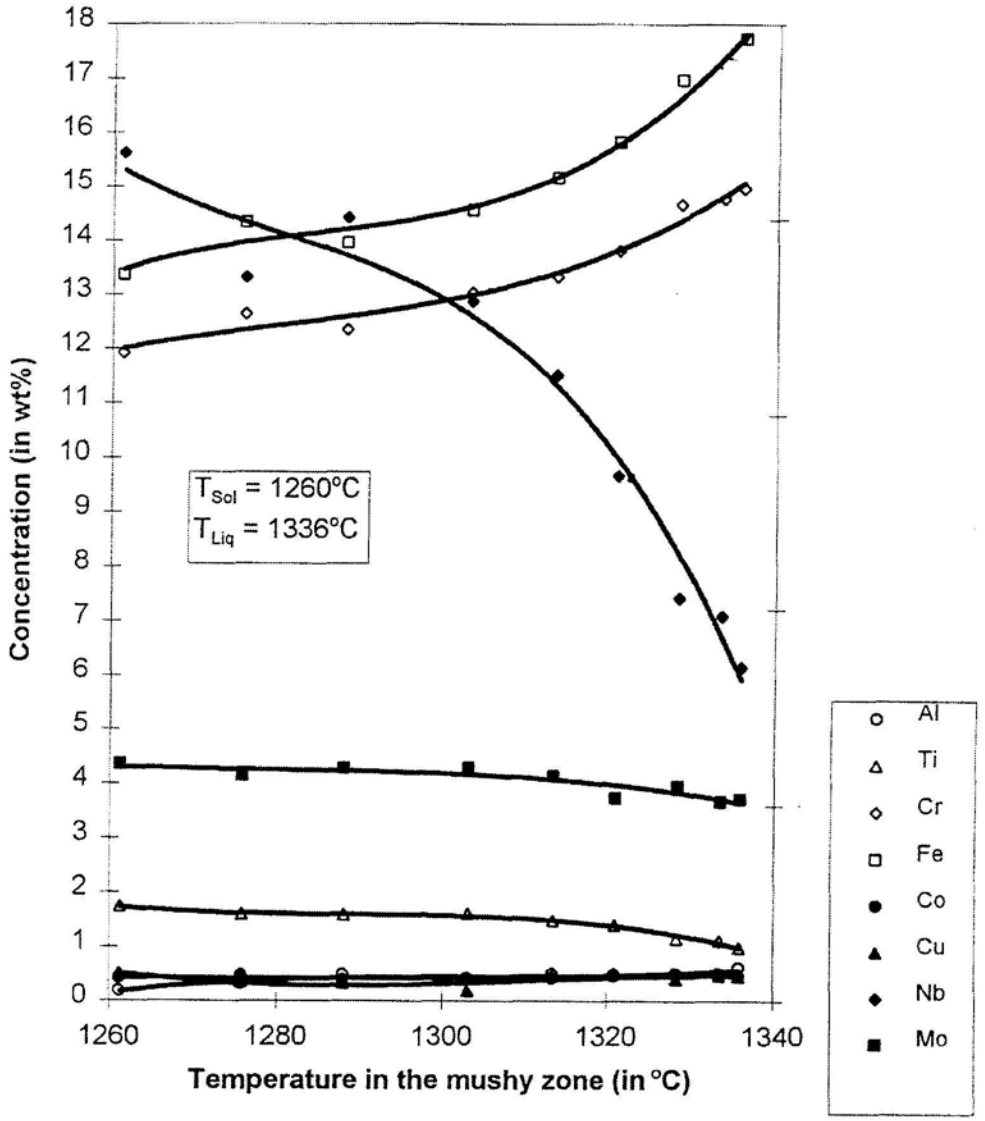

Figure 4.3 Interdendritic liquid segregation in Inconel 718 [50]

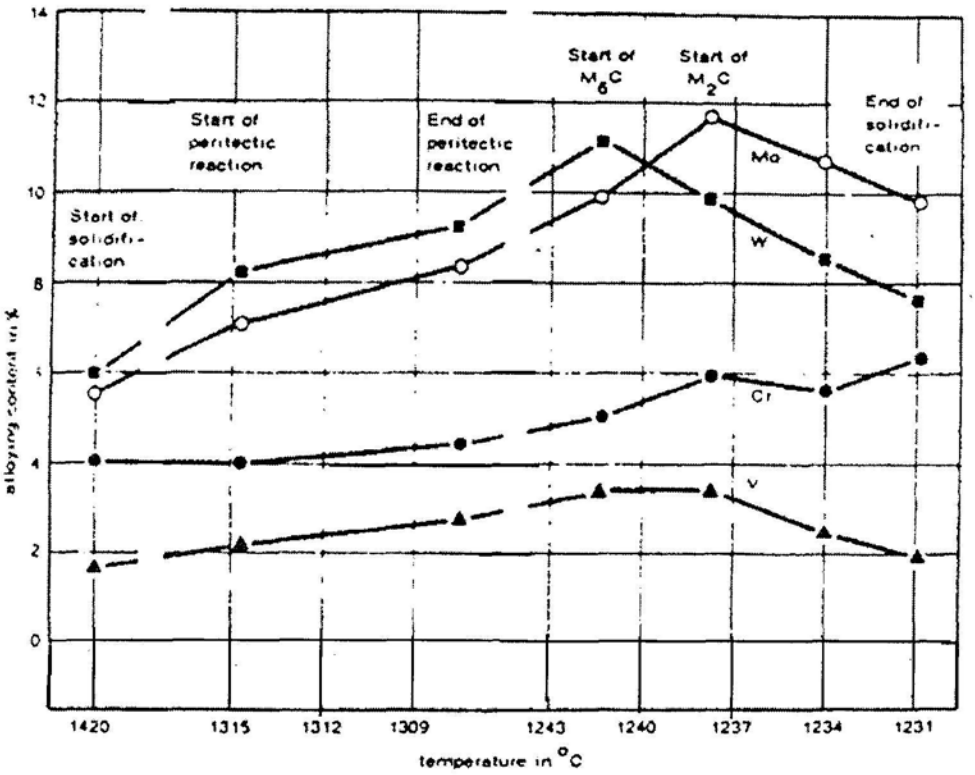

Figure 4.4 The equilibrium solidification of M2 steel [50]

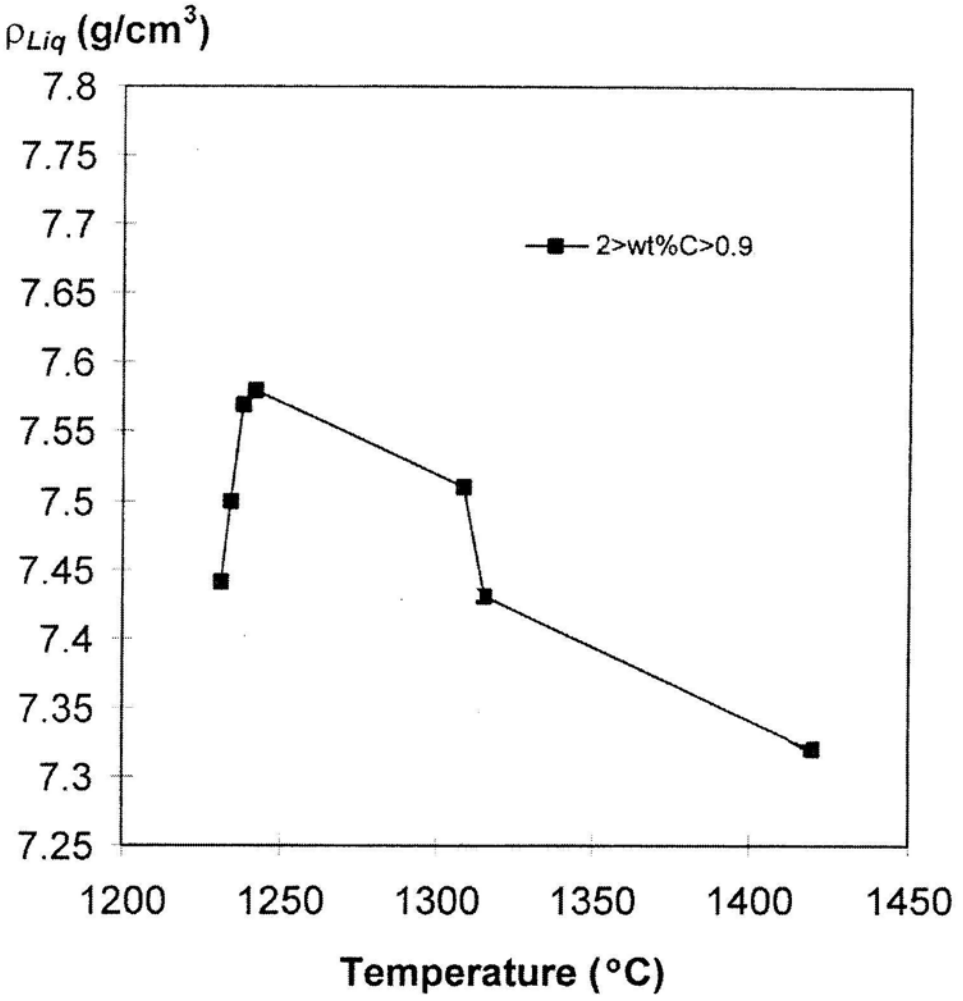

Figure 4.5 Interdendritic liquid density in M2 steel (0.9<wt% C<2) [50]

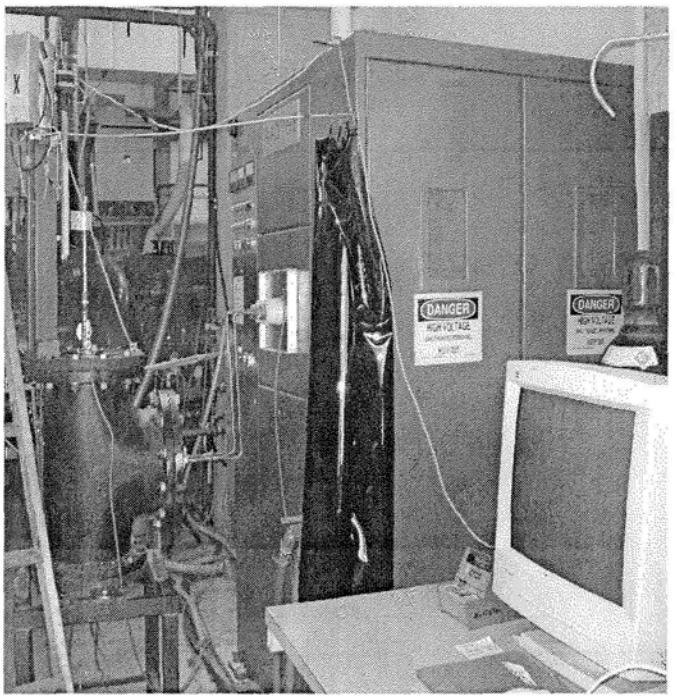

Figure 4.6 Apparatus of the DSQ furnace and its affiliate

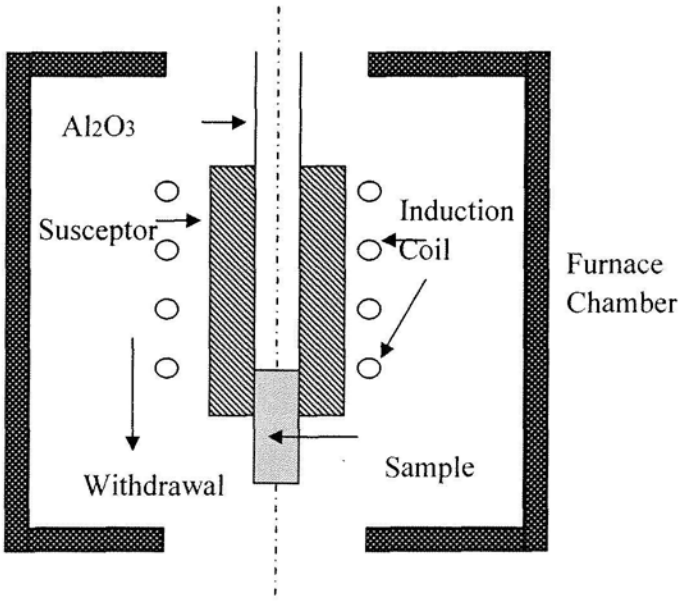

Figure 4.7 A schematic drawing of the DS/DSQ furnace

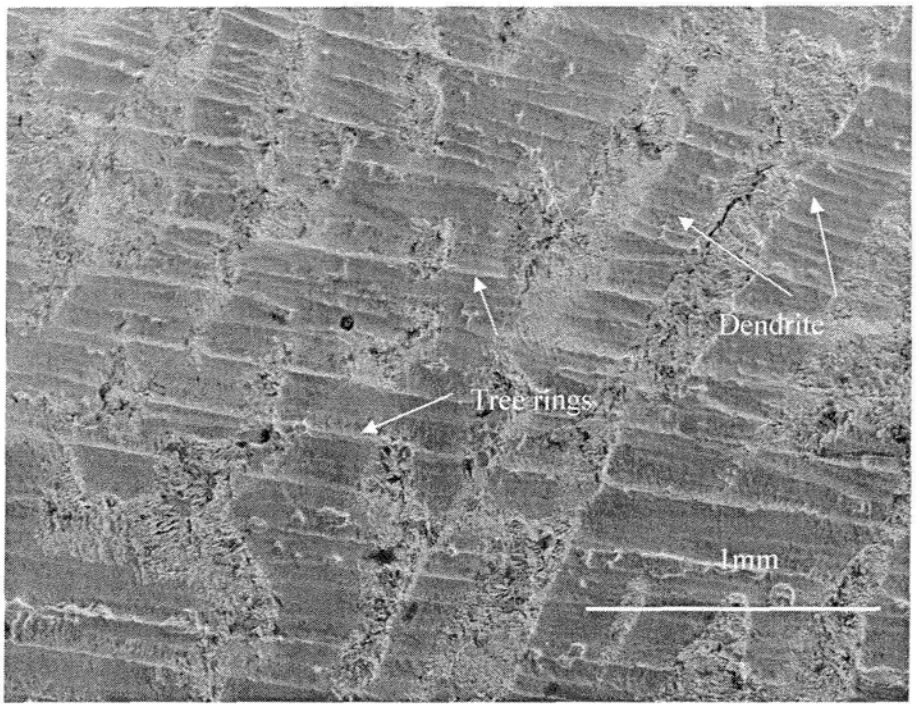

Figure 5.1 Tree rings in the industrial Inconel 718 ingot (SEM image)

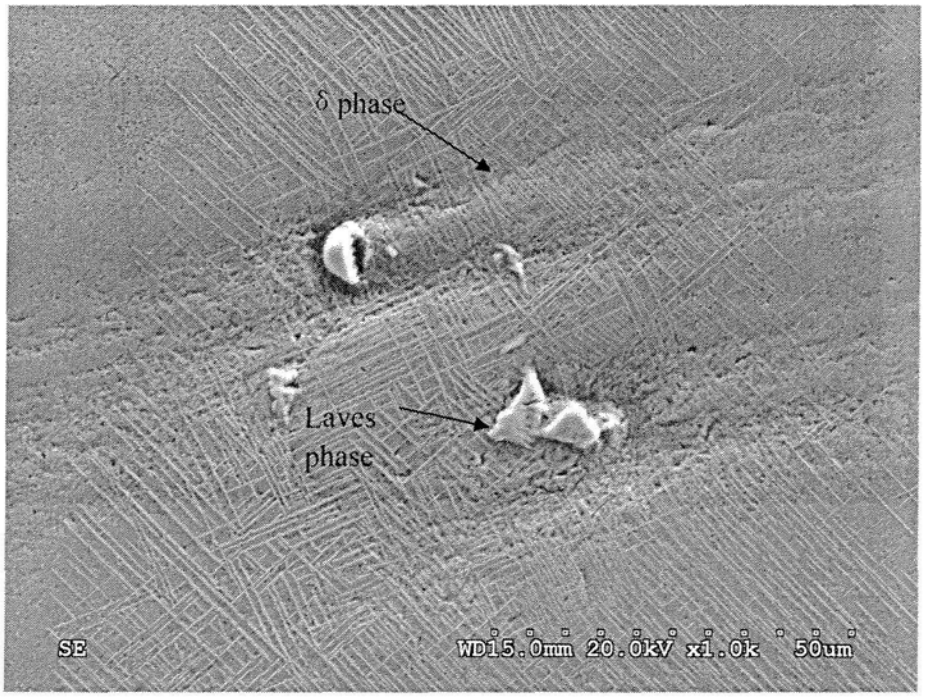

Figure 5.2 Laves phase and delta phase combination in the industrial Inconel 718 ingot(SE image)

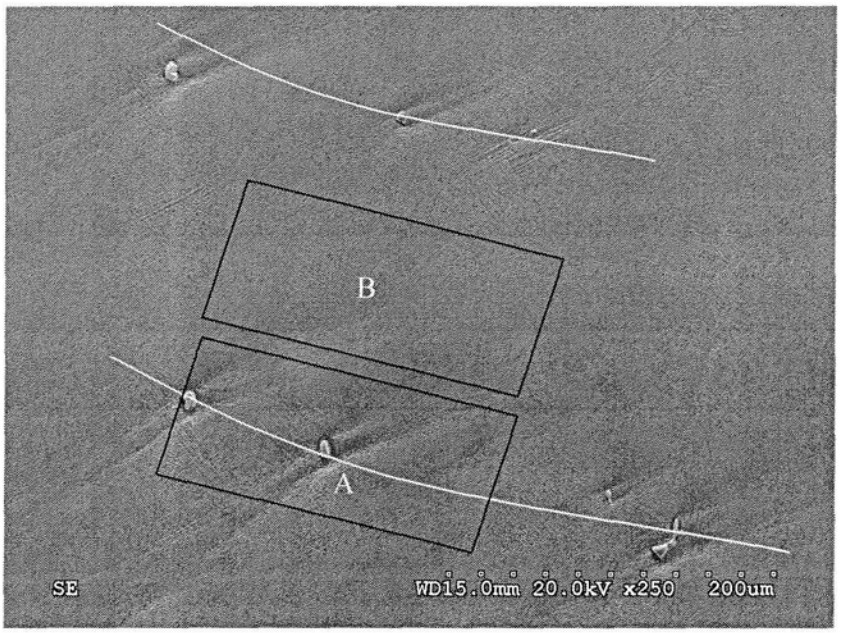

Figure 5.3 Laves phase and δ phase combination in industrial Inconel 718. White curves refer to the tree rings structures(SE image)

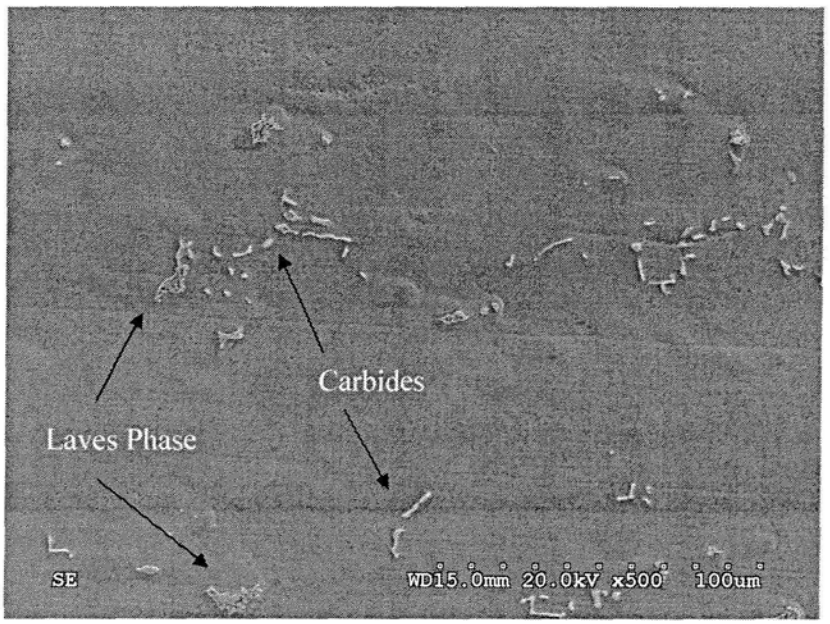

Figure 5.4 Inconel 718-DS (directional solidified) specimen (SE image)

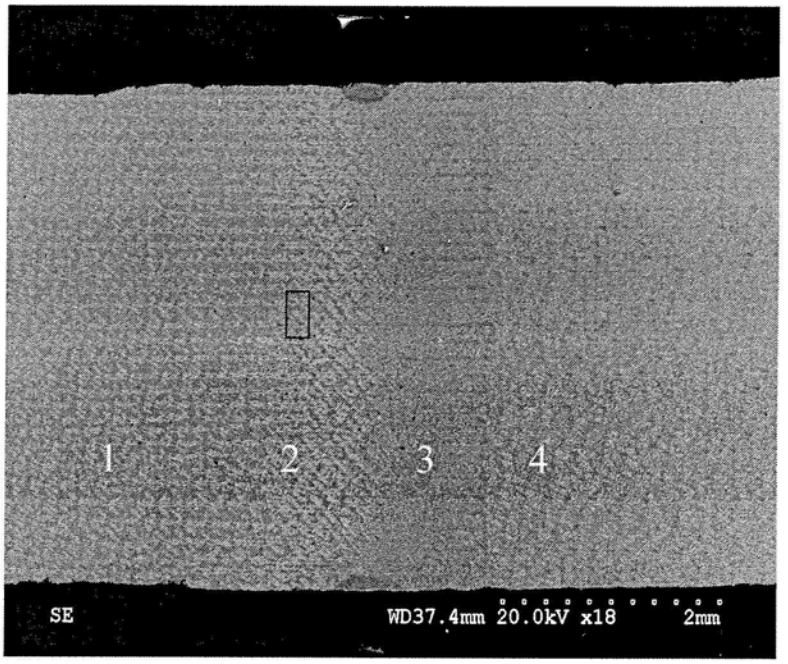

Figure 5.5 Band observed in Inconel 718-E sample (Band corresponds to a combination of zone 2 and zone 3; The rectangular stands for the scanning area)

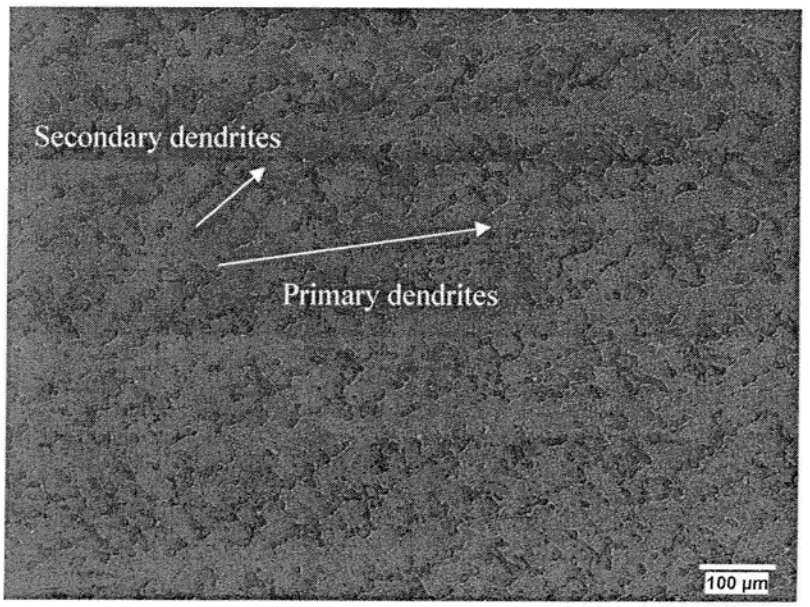

Figure 5.6 Dendrite structure in normal growth region (zone1 in Figure 3-2) of Inconel 718-E (optical micrograph)

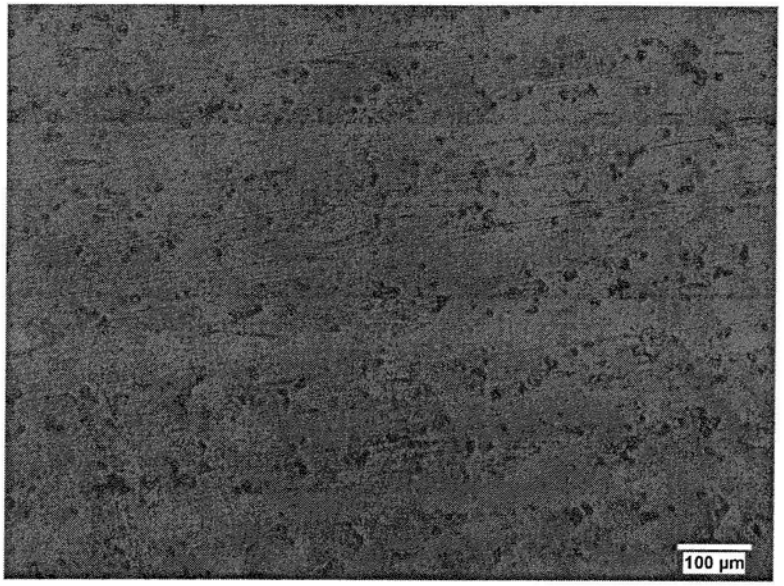

Figure 5.7 Dendrite structure in interrupted region (zone2 in Figure 3-2) of Inconel 718-E (optical micrograph)

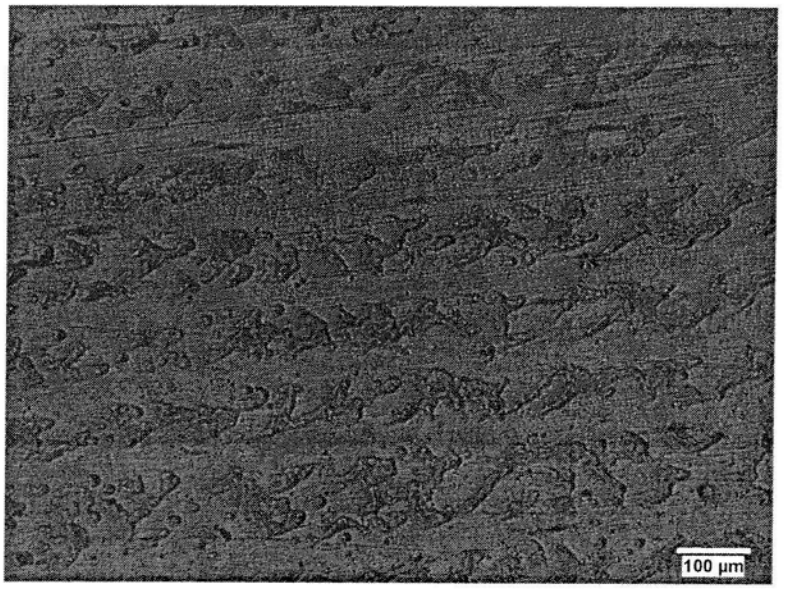

Figure 5.8 Dendrite structure in the interrupted region (zone3 in Figure 3-2) of Inconel 718-E(optical micrograph)

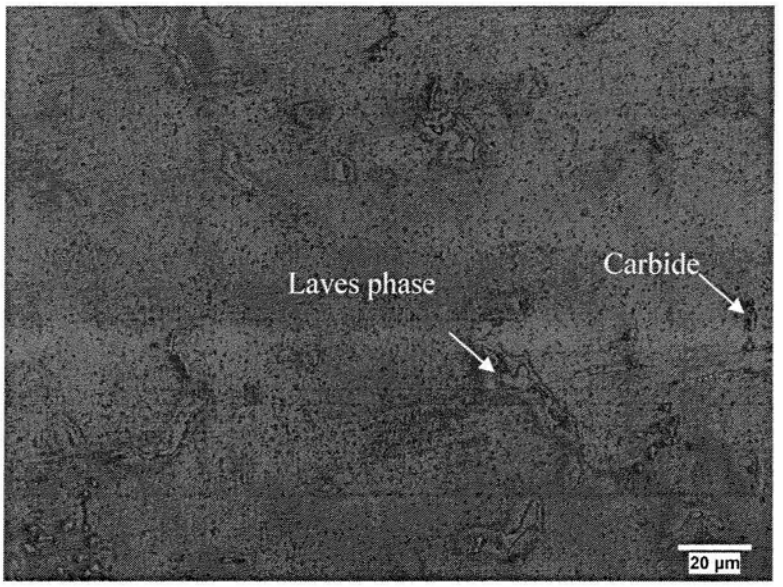

Figure 5.9 Microstructures in zone 1, Inocnel 718-E (optical micrograph)

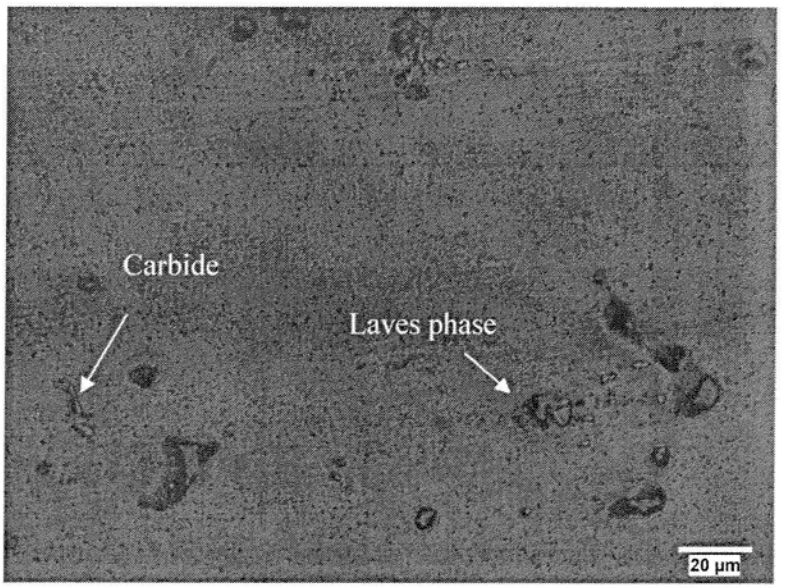

Figure 5.10 Microstructure in zone 2, Inconel 718-E (optical micrograph)

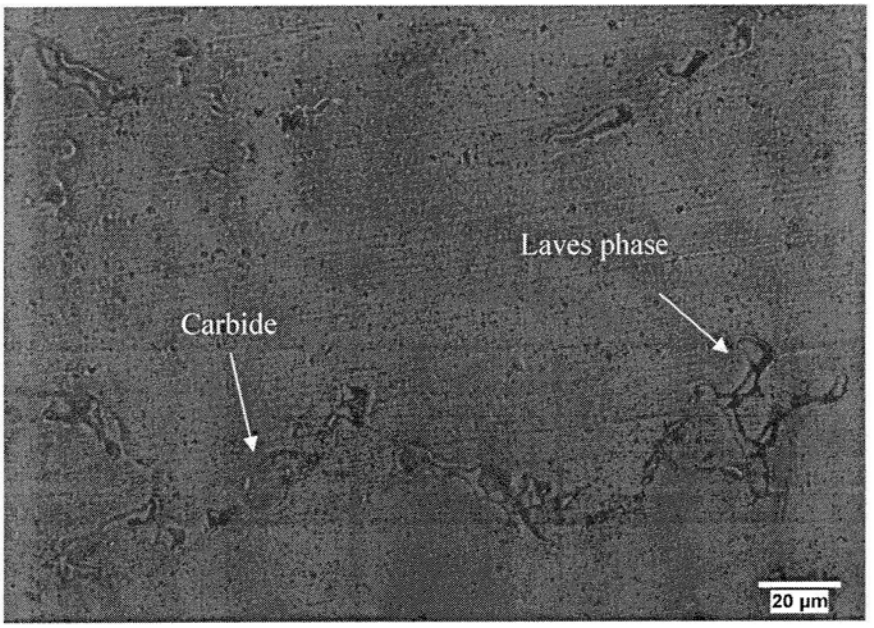

Figure 5.11 Microstructure in zone 3, Inconel 718-E (optical micrograph)

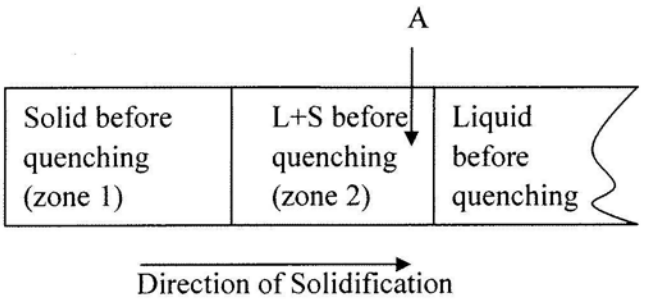

Figure 5.12 Schematic description on Inconel 718 quenched specimen. Arrow A indicates the location where Figures 5.13 and 5.14 were taken.

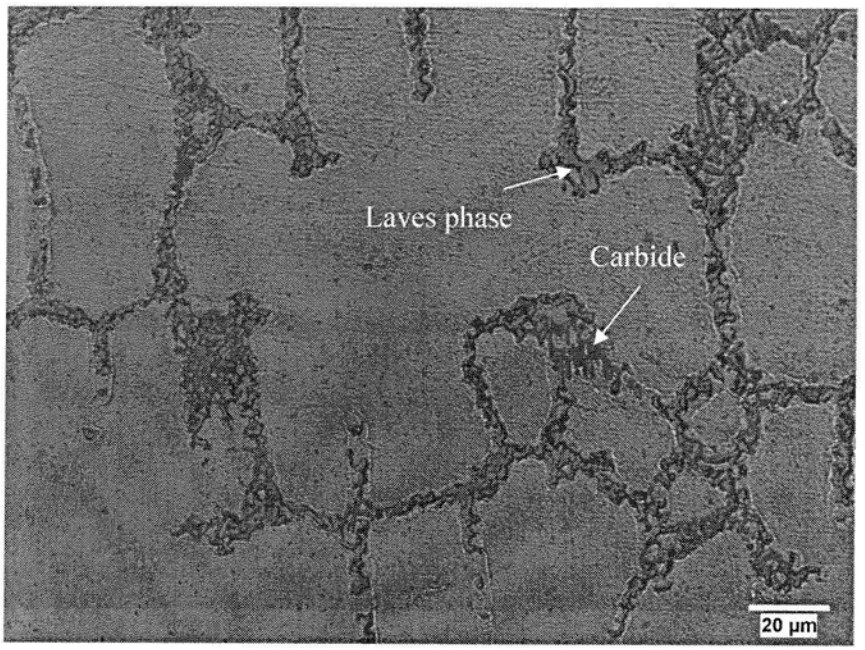

Figure 5.13 Microstructure in zone 2 of Inconel 718-EQ (optical micrograph)

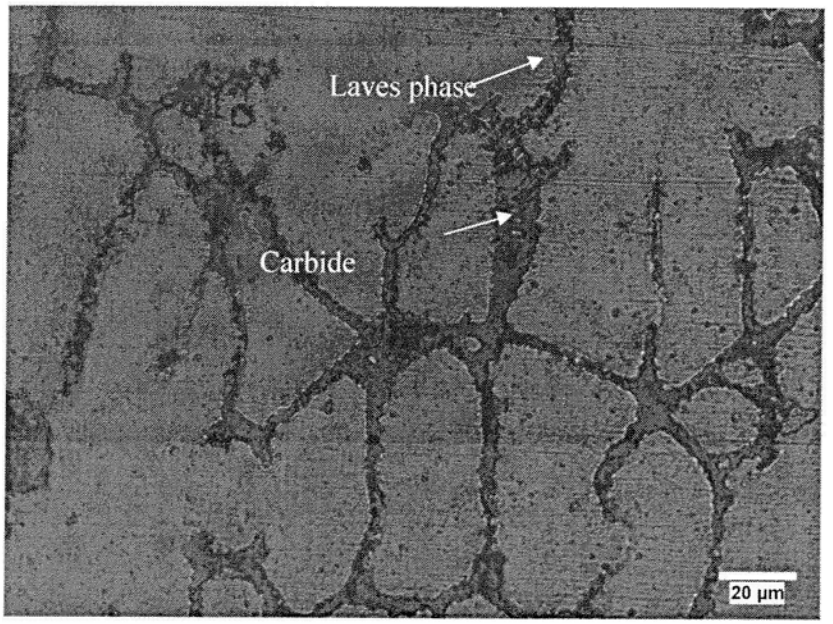

Figure 5.14 Microstructure in zone 2 of Inconel 718-EWQ (optical micrograph)

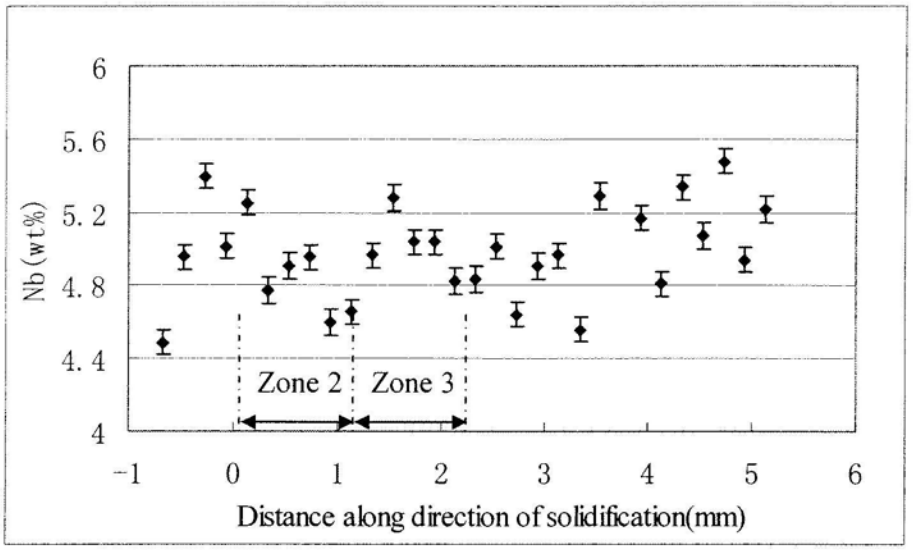

Figure 5.15 Bulk Nb compositional analysis of Inconel 718-E sample (zero on the x-axis is the beginning of zone 2, the error bars stand for the errors coming from the EDX analysis)

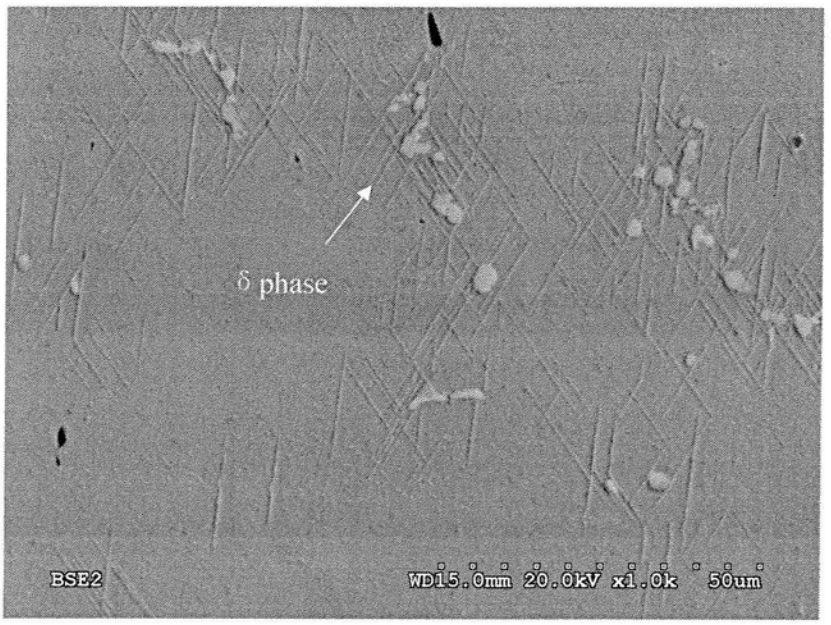

Figure 5.16 Inconel 718-E heat treated sample (BSE image)

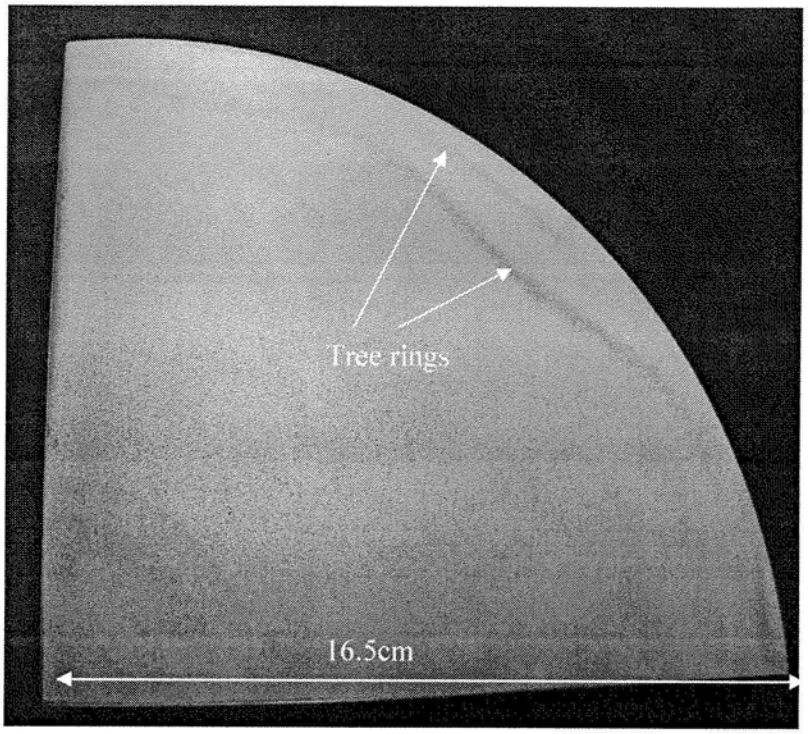

Figure 5.17 Banding in the industrial Waspaloy ingot

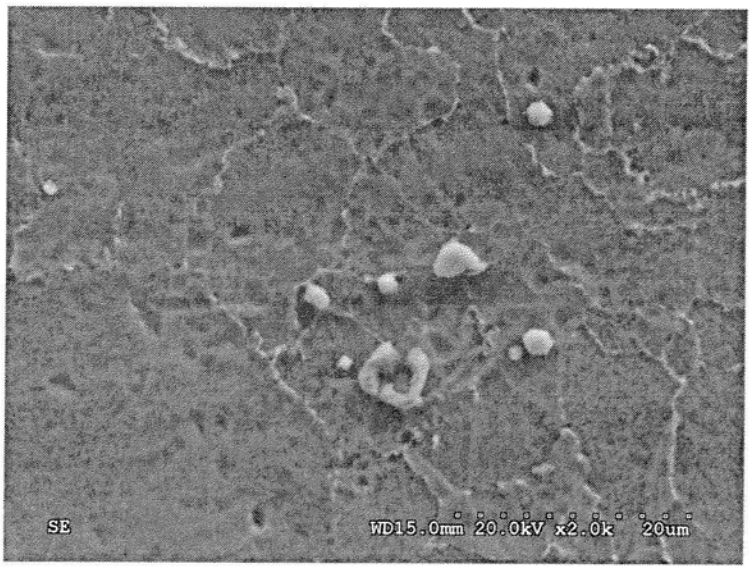

Figure 5.18 The precipitates inside the banded region in the industrial Waspaloy (SE image)

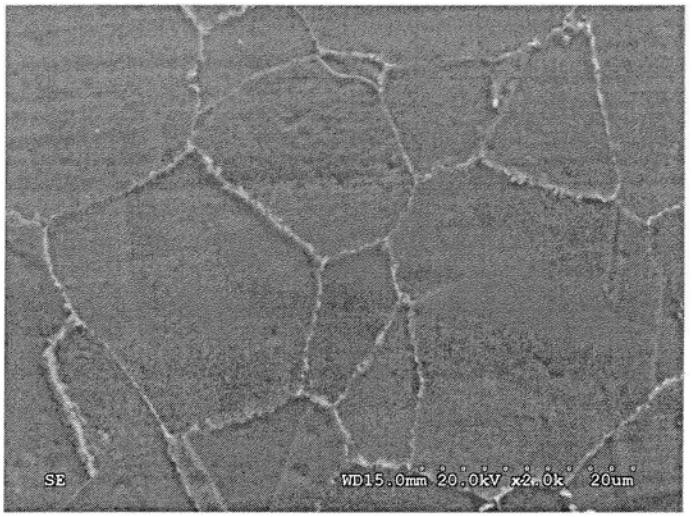

Figure 5.19 Outside of the banded region in the industrial Waspaloy sample (SE image)

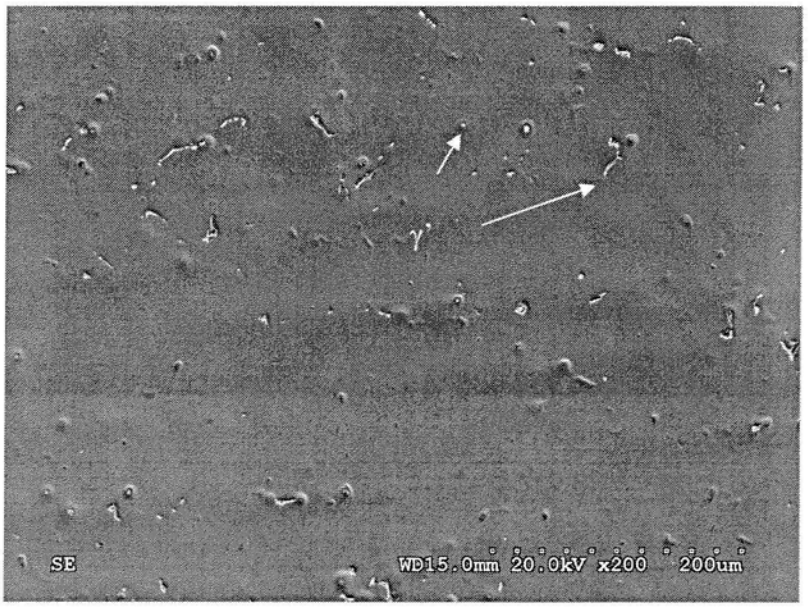

Figure 5.20 Nimonic 80A, specimen E, morphology of normal growth region (zone 1, SE image)

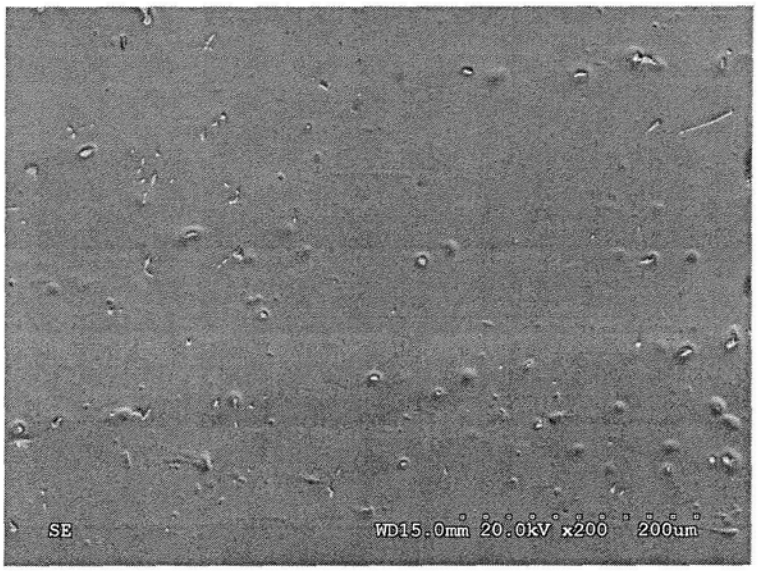

Figure 5.21 Nimonic 80A, specimen E, morphology of interrupted region (zone2, SE image)

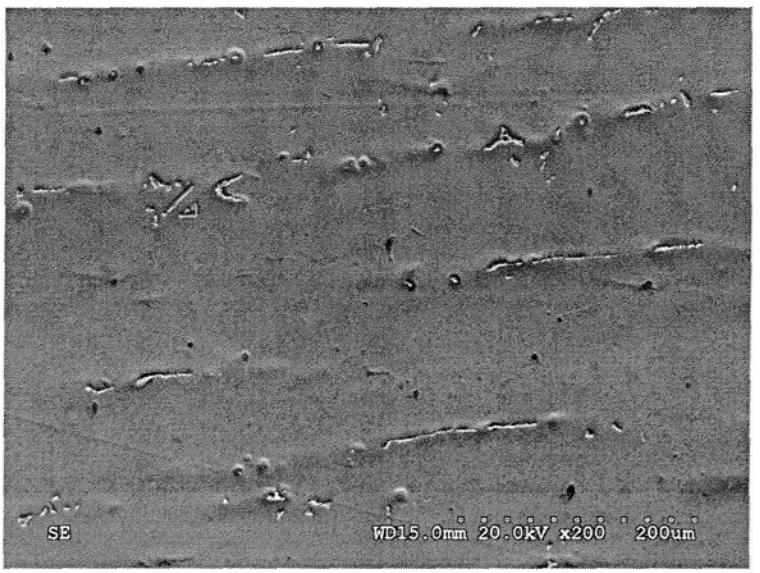

Figure 5.22 Nimonic 80A, specimen E, morphology of interrupted region (zone 3, SE image)

Figure 5.23 Waspaloy, specimen E morphology of normal growth region (zone 1, SE image)

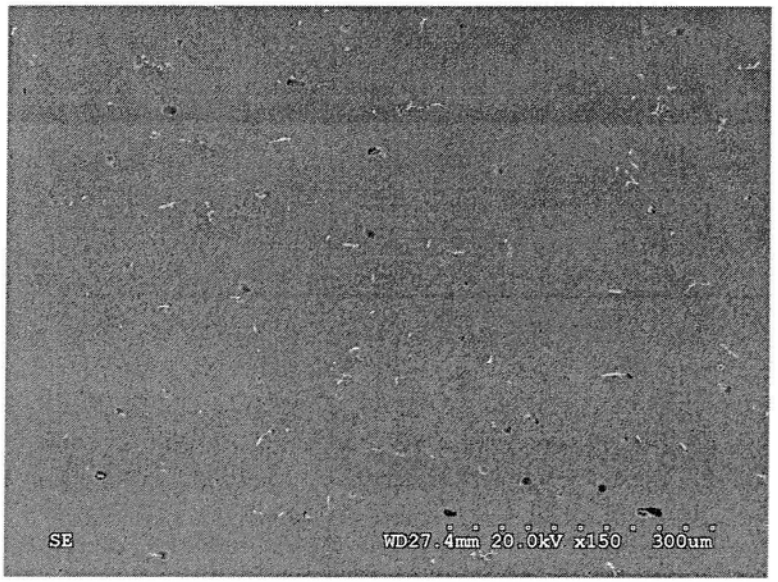

Figure 5.24 Waspaloy, specimen E, morphology of interrupted region (zone 2, SE image)

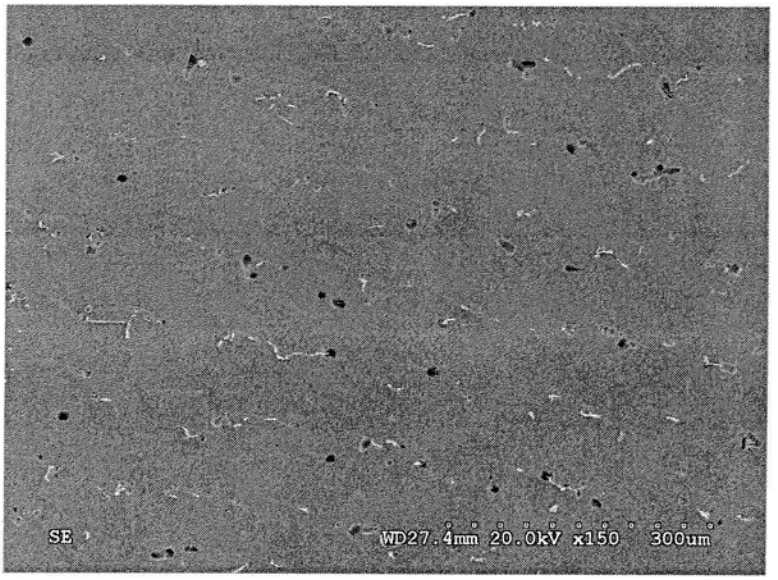

Figure 5.25 Waspaloy, specimen E, morphology of interrupted region (zone 3, SE image)

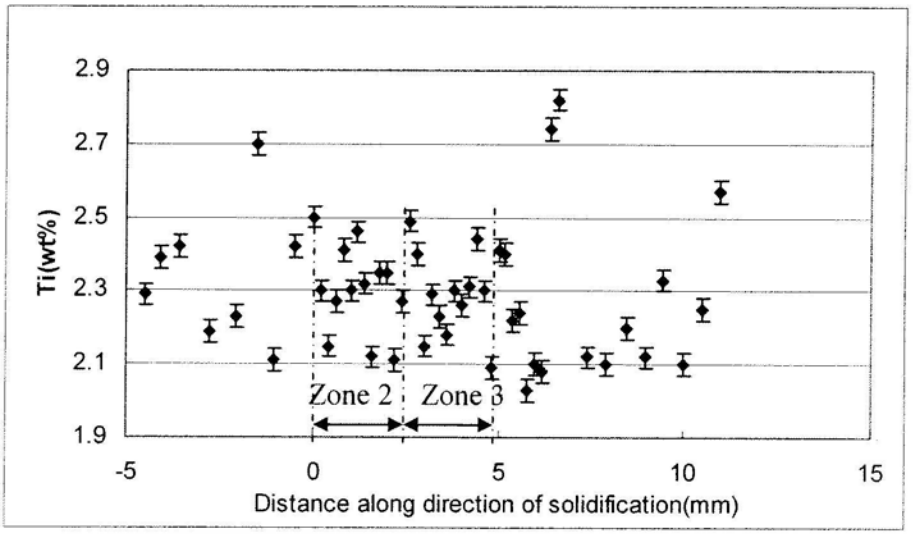

Figure 5.26 Bulk Ti concentration vs. axial distance for Nimonic80 A-E specimen (axis 0 indicates the beginning of zone 2, the error bars stand for the errors coming from the EDX anlysis)

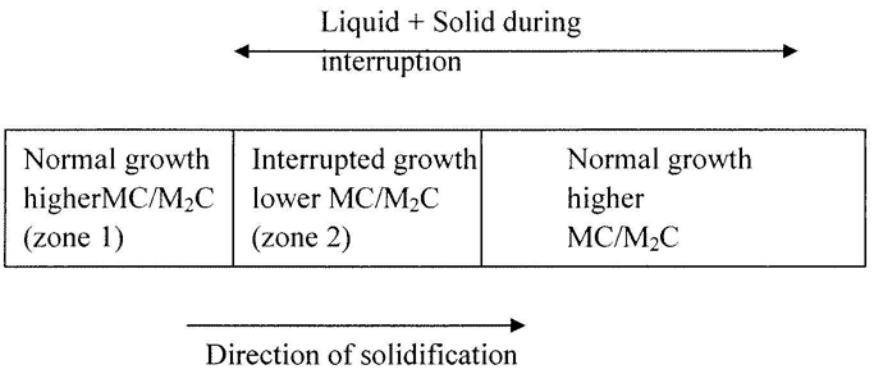

Figure 5.27 Schematic descriptions of different zones of M50-E specimen

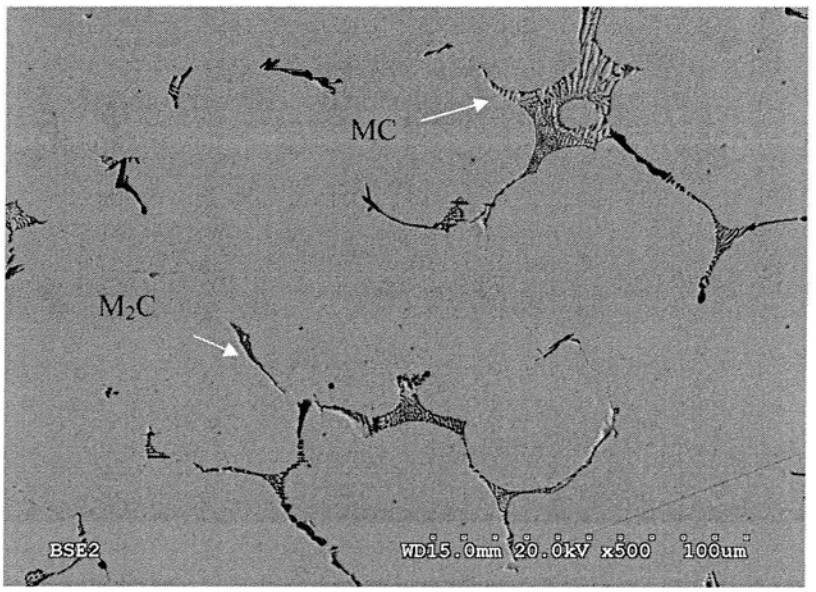

Figure 5.28 Carbide Morphology of M50-E, normal growth region (bottom, BSE image)

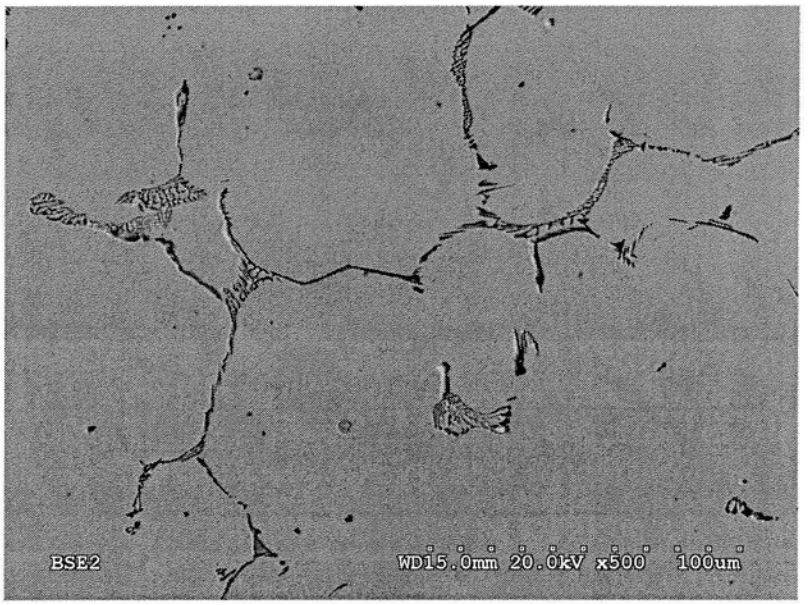

Figure 5.29 Carbide morphology of M50-E, interrupted growth (BSE image)

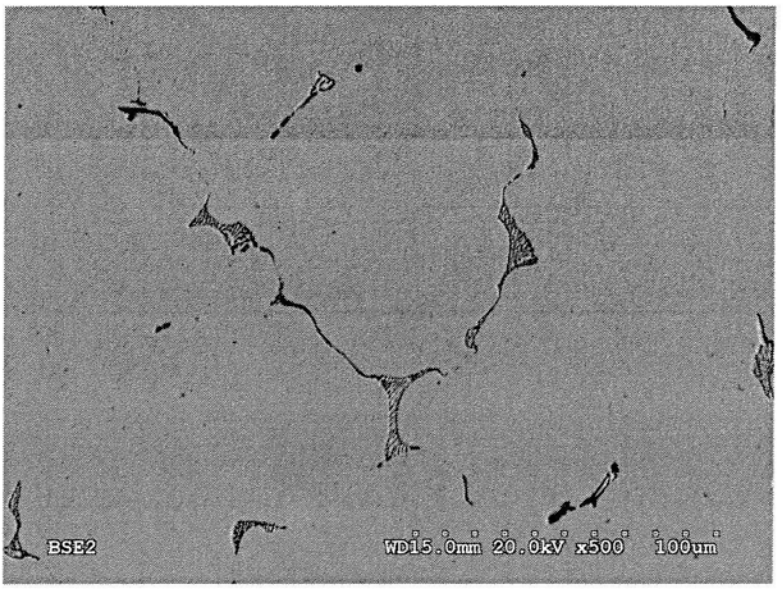

Figure 5.30 Carbide morphology of M50-E, normal growth region (top, BSE image)

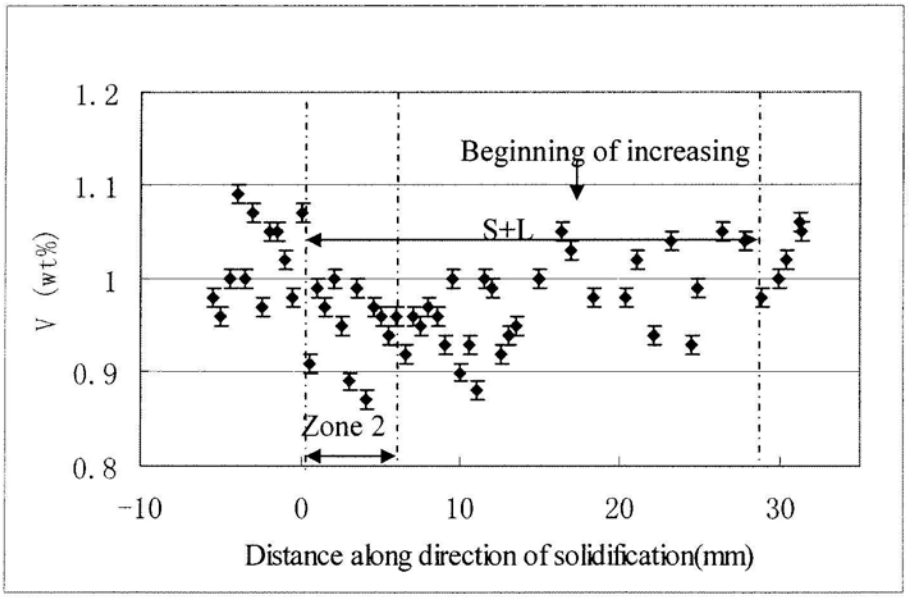

Figure 5.31 Bulk vanadium concentration of M50-E with distance (zero along the x-axis indicates the beginning of zone 2, the error bars stand for the errors coming from the EDX anlysis)

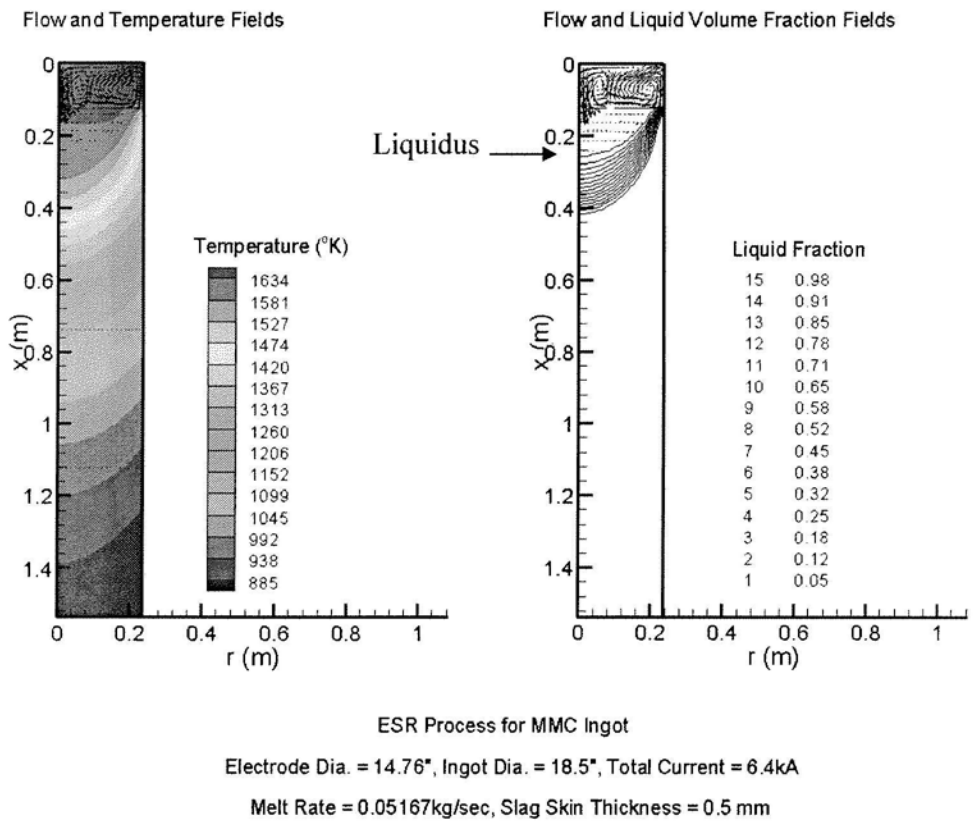

Figure 6.1 Flow fields during the ESR process for MMC ingot

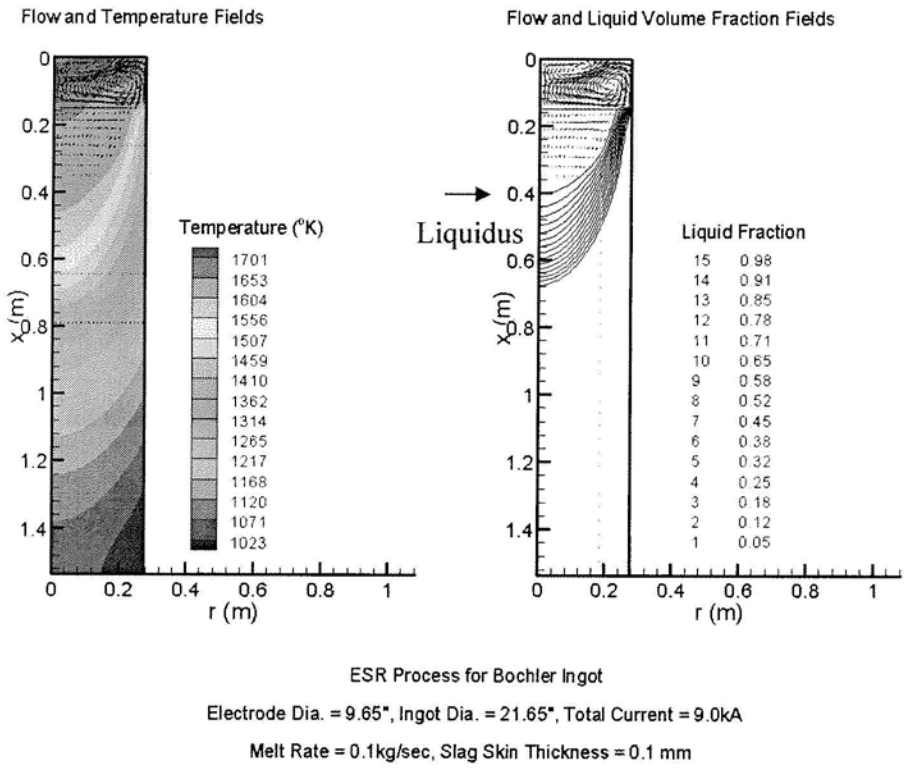

Figure 6.2 Flow field during the ESR process for Bochler ingot

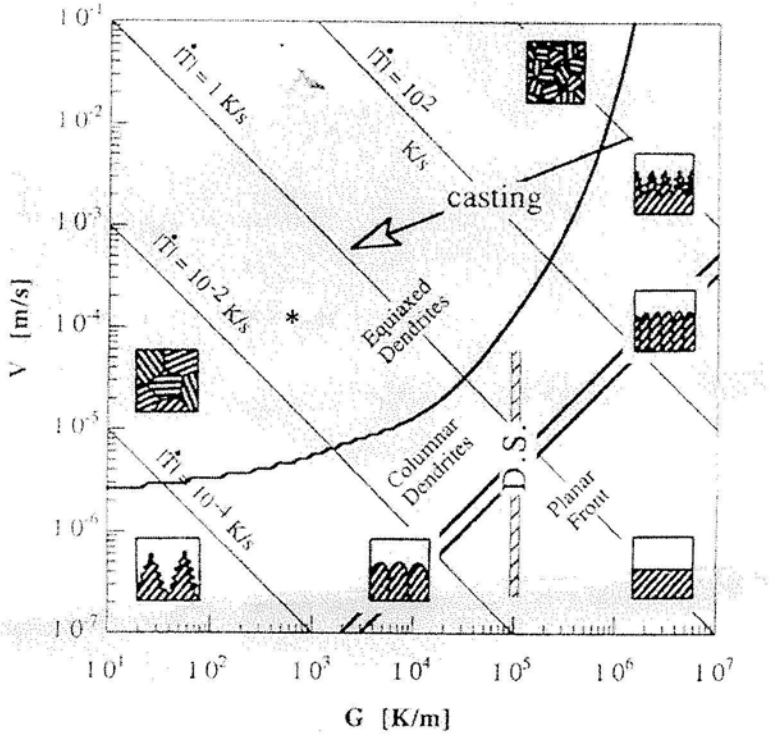

Figure 6.3 Schematic Summary of Single-Phase Solidification Morphologies[59]

(Asterisk shows the position in the present DS experiments)

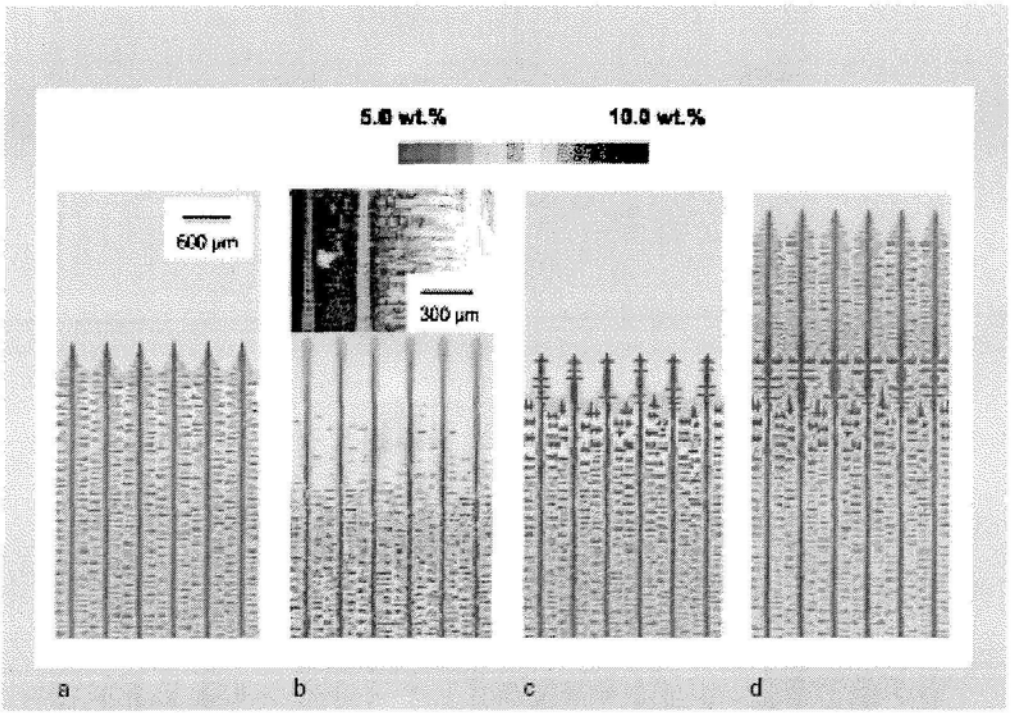

Figure 6.4 Predicted microstructures during seed melt-back with flat isotherms: (a) seed, (b) melt-back, and (c,d) at 20 s and 45 s after withdrawal started [61]

Bibliography

1. G. Krauss, Metall Mater Trans B, 2003, Vol 34B, pp 718-792

2. R. L. Cairns, J. A. Charles, Iron and Steel, 1966, pp 511-517

3. F. Thompson and R. Willows, JISI, 1931, Vol 124, pp 151-154

4. X. Xu, R. M. Ward, M. H. Jacobs and P. D. Lee, Metall Mater Trans A, 2002, Vol 33, pp 1795-1804

5. J. D. Lavender and F.W. Jones, JISI, 1949, Vol 163, pp 14-17

6. W. Kurz and R. Trivedi, Metall Mater Trans A, 1996, Vol 27A, pp 625-631

7. R. Trivedi, Metall Mater Trans A, 1995, Vol 26A, pp 1583-1590

8. S. Sawa, S. Shibuya, S. Kinbara, Proceedings 4th IGVM, Section 2, 1974, pp 129-134

9. J. E. Stead, JISI, 1918, Vol 97 pp 287-295

10. H. Brearley, W. H. Hatfield, Abstract, JISI, 1918, Vol 97 pp 293-294

11. J. H. Whitely, JISI, 1926, Vol 113, pp 213-218

12. E. F. Jatczak, D. J. Girardi and E. S. Rowland, Trans ASM, 1952, Vol 48, pp 279-303

13. P. G. Bastien, JISI, 1957, Vol 187, pp 281-291

14. J. Kirkaldy, J. Destinon-Forstmann and R. Brigham, Canadian Metallurgical Quarterly, 1962, Vol 1, pp 14-18

15. S. Thompson and P. Howell, Mater Sci Tech, 1992, Vol 8, pp 777-784

16. R. O. Jackson M.A.Sc. Thesis, UBC, 1972

17. G. L. Jia, G. Z. Zhang, X. J. Li, Y. J. Qiao and Y. Y. Gao, J Northeast Univ Mater Sci, 1994, Vol 15, pp 290-293

18. M. Murgas, M. Pokusova and A. Pokusa, Research on the problem of stirring in the continuous casting of steel, Hutnicke Litsty, 2001, Vol 56, no. 1-3, pp 7-12.

19. N. A Shah, J. More, Iron and Steelmaker Oct 1982, pp 31-34

20. C. Bernhard, M. Lechner, M. Forsthuber, and E. Doringer, Numerical simulation of solidification in continuous casting of rounds

21. J. Casey, Macro-etching of Continuous cast steel, Microscopy Society of America, 2002

22. M. R. Bridge, G. D. Rogers, Metall Trans B, 1984, Vol 15B, pp 581-586

23. J. Beech, Journal of Crystal Growth, 1984, Vol 67, pp 385-390

24. F. Zanner, R. Williamson, R. Erdmann, Proceedings of LMPC, 2005, pp 13-19

25. H. Schwatzbart, Trans ASM, 1952, Vol 44, pp 845-852

26. W. Owen, D. Whitmore, M. Cohen and B. Averbach, The Welding Journal Research Supplement, 1957, pp 503-512

27. R. A. Grange, Metall Trans, 1971, Vol 2, pp 417-426

28. F. A. Heiser and R.W. Hertzberg, JISI, 1971, Vol 209, pp 975-980

29. G. R. Rao, E. H. Lee and B. A. Chin, Surface and Coatings Technology, 1992, Vol 51, pp 112-117

30. A. C. Stauffer, D. A. Koss, and J. B. Mckirgan, Metall Mater Trans A, 2004, Vol 35A, pp 1317-1324

31. G. Hoyle, Electroslag processes principles and practice,1983, Applied Science Publishers

32. S. V. Joshi, Ph.D. Thesis, UBC 1971

33. A. Mitchell, Process parameters in ESR and VAR as applied to superalloy melting, unpublished

34. A. Mitchell, Material Science and Engineering A, 2005, Vol 413-414, pp 10-18

35. A. Jardy, L. Falk and D. Abitzer, Ironmaking and Steelmaking, 1992, Vol 19, pp 226-232

36. A. D. Patel, Liquid Metals Processing and Casting 2003, pp 205-213

37. A. Mitchell and S. Joshi, Metall Transactions, 1973, Vol 4, pp 631-642

38. B. Hernandez-Morales and A. Mitchell, Iron and Steelmaking,1999, Vol 26, pp 423-438

39. A. S. Ballantyne, Ph.D. thesis, UBC, 1978

40. K. M. Kelkar, S. V. Patankar, A. Mitchell, O. Kanou, N. Fukada, K. Suzuki, Computational modeling of the Vacuun Arc Remelting Process used for the production of Ingots of Titanium Alloys, 2006, Report

41. K. M. Kelkar, Computational analysis of electroslag remelting and vaccum arc remelting process used for the production of high-performance alloys, presentation at Innovative Research

42. P. Auburtin, Ph.D. thesis, UBC, 1998

43. M. McLean, Directionally Solidified Materials for High Temperature Service, 1983, The Metals Society, London

44. M. J. Donachie and S. J. Donachie, Superalloys-A technical Guide, ASM, 2002

45. ASM Handbook, Vol 10

46. A. Formenti, A. Eliasson, A. Mitchell and H. Fredriksson, High temperature materials and processes, 2005, Vol 24, pp 239-258

47. M. Abdellaoui, C. Slama, Journal of Alloys and Compounds, 2000, Vol 306, pp 277-284

48. Y. Desvallees, M. Bouzidi, F. Bois and N. Beaude, Superalloys 1994, TMS, pp 281-291

49. T. Antonsson and H. Fredriksson, Metall Mater Trnas B, 2005, Vol 36B, pp 85-96

50. P. L Auburtin, M.A.Sc thesis, UBC, 1995

51. W. Betteridge and J. Heslop, The Nimonic alloys, 1974, Crane, Russak & Company

52. Report, Special Metals Corporation, 2004

53. Y. Murata, M. Morinaga, N. Yukawa, H. Ogawa and M. Kato, Proceeding of The first Pacific Rim International Conference of Advanced Materials, 1992, pp 269-274

54. C. Djega-Mariadassou, B. Decaudin, L. Bessais and G. Cizerron, J Phys Mater, 1997, Vol 9, pp 4931-4942

55. B. Decaudin, C. Djega-Mariadassou and G. Cizerron, Journal of Alloys and Compounds, 1995, pp 208-212

56. A. S. Ballantyne and A. Mitchell, Proceeding of Solidification and Casting of Metals, 1977, Metals Society, pp 363-370

57. P. Auburtin, T. Wang, S. L. Cockcroft, and A. Mitchell, Metall Mater Trans B, 2001, Vol 31, pp 801-811

58. K. M. Kelkar, J. Mok, S. V. Patankar and A. Mitchell, Computational Modelling of Electroslag Remelting Process, J Phys IV, 2004, pp 421-428

59. W. Kurtz and D. J. Fisher, Fundamentals of Solidification, 1989, Trans Tech Publications, p 88

60. T. Wang, M.A.Sc thesis, UBC, 2000

61. X. L. Yang, P. D. Lee and N. D'Souza, Journal of Materials, 2005, Vol 57, pp 40-44